

H $\alpha$  SPECTROSCOPY OF GALAXIES AT  $z > 2$ : KINEMATICS AND STAR FORMATION<sup>1</sup>DAWN K. ERB, ALICE E. SHAPLEY, CHARLES C. STEIDEL<sup>2</sup>

California Institute of Technology, Department of Astronomy, MS 105-24, Pasadena, CA 91125

MAX PETTINI

Institute of Astronomy, Madingley Road, Cambridge CB3 0HA, UK

KURT L. ADELBERGER<sup>3</sup>

Harvard-Smithsonian Center for Astrophysics, 60 Garden Street, Cambridge, MA 02138

MATTHEW P. HUNT

California Institute of Technology, Department of Astronomy, MS 105-24, Pasadena, CA 91125

ALAN F.M. MOORWOOD

European Southern Observatory, Karl-Schwarzschild-Str. 2, D-85748 Garching, Germany

AND

JEAN-GABRIEL CUBY

European Southern Observatory, Alonso de Cordova 3107, Santiago, Chile

Accepted for publication in ApJ

## ABSTRACT

We present near-infrared spectroscopy of H $\alpha$  emission lines in a sample of 16 star-forming galaxies at redshifts  $2.0 < z < 2.6$ . Our targets are drawn from a large sample of galaxies photometrically selected and spectroscopically confirmed to lie in this redshift range. We have obtained this large sample with an extension of the broadband  $U_nG\mathcal{R}$  color criteria used to identify Lyman break galaxies at  $z \sim 3$ . The primary selection criterion for IR spectroscopic observation was proximity to a QSO sight-line; we therefore expect the galaxies presented here to be representative of the sample as a whole. Six of the galaxies exhibit spatially extended, tilted H $\alpha$  emission lines; rotation curves for these objects reach mean velocities of  $\sim 150$  km s $^{-1}$  at radii of  $\sim 6$  kpc, without corrections for inclination or any other observational effect. The velocities and radii give a mean dynamical mass of  $\langle M \rangle \geq 4 \times 10^{10} M_{\odot}$ . We have obtained archival *HST* images for two of these galaxies; they are morphologically irregular. One-dimensional velocity dispersions for the 16 galaxies range from  $\sim 50$  to  $\sim 260$  km s $^{-1}$ , and in cases where we have both virial masses implied by the velocity dispersions and dynamical masses derived from the spatially extended emission lines, they are in rough agreement. We compare our kinematic results to similar measurements made at  $z \sim 3$ , and find that both the observed rotational velocities and velocity dispersions tend to be larger at  $z \sim 2$  than at  $z \sim 3$ . We also calculate star formation rates (SFRs) from the H $\alpha$  luminosities, and compare them with SFRs calculated from the UV continuum luminosity. We find a mean  $SFR_{H\alpha}$  of  $16 M_{\odot} \text{ yr}^{-1}$  and an average  $SFR_{H\alpha}/SFR_{\text{UV}}$  ratio of 2.4, without correcting for extinction. We see moderate evidence for an inverse correlation between the UV continuum luminosity and the ratio  $SFR_{H\alpha}/SFR_{\text{UV}}$ , such as might be observed if the UV-faint galaxies suffered greater extinction. We discuss the effects of dust and star formation history on the SFRs, and conclude that extinction is the most likely explanation for the discrepancy between the two SFRs.

*Subject headings:* galaxies: evolution — galaxies: high-redshift — galaxies: kinematics and dynamics — galaxies: starburst — infrared: galaxies

## 1. INTRODUCTION

Our knowledge of star-forming galaxies at high redshift has increased enormously in the past ten years, particularly at  $z \sim 3$ ; large samples of galaxies at these redshifts are now known (Steidel et al. 1999, 2003), and they have been studied in both the rest-frame UV (Pettini et al. 2000; Shapley et al. 2003) and optical (Shapley et al. 2001; Papovich, Dickinson, & Ferguson 2001; Pettini et al. 2001), as well as at submillimeter (Chapman et al. 2000; Adelberger & Steidel 2000) and X-ray (Nandra et al. 2002) wavelengths to some extent. Much less is known about galaxies at  $z \sim 2$ . Because these objects lack strong spectroscopic features in the optical window, they have

traditionally been difficult to identify. This is unfortunate, as  $z \sim 2$  is likely the epoch in which a large fraction of the stars in the present day universe formed (Madau, Pozzetti, & Dickinson 1998; Blain et al. 1999), in which bright QSO activity reached its peak (Schmidt, Schneider, & Gunn 1995; Pei 1995; Fan et al. 2001), and in which rapidly star-forming galaxies of compact and disordered morphologies became the normal Hubble sequence galaxies of the  $z < 1$  universe (Dickinson 2000).

The situation is improving, however. With the advent of sensitive IR detectors observations of rest-frame optical features are now feasible, and have been carried out successfully. Teplitz, Malkan, & McLean (1998) reported 11 H $\alpha$  emitters discovered in a narrow-band IR imaging survey; Yan et al.

<sup>1</sup>Based, in part, on data obtained at the W.M. Keck Observatory, which is operated as a scientific partnership among the California Institute of Technology, the University of California, and NASA, and was made possible by the generous financial support of the W.M. Keck Foundation. Also based in part on observations collected at the European Southern Observatory, Paranal, Chile (ESO Programme 66.A-0206).

<sup>2</sup>Packard Fellow

<sup>3</sup>Harvard Society Junior Fellow

(1999) and Hopkins, Connolly, & Szalay (2000) used slitless spectroscopy with the Near Infrared Camera and Multi-Object Spectrograph (NICMOS) on the *Hubble Space Telescope (HST)* to study the  $\text{H}\alpha$  luminosity function and star formation rate in galaxies at  $z \leq 1.9$ . Objects at  $z \sim 2$  are in fact ideally suited for ground-based IR spectroscopy, since  $\text{H}\alpha$  falls in the  $K$ -band,  $[\text{O III}]$  and  $\text{H}\beta$  in the  $H$ -band, and  $[\text{O II}]$  in the  $J$ -band. This coincidence has been exploited with recent observations employing near-IR spectrographs on 8–10 m telescopes; most of these have focused on  $\text{H}\alpha$  emission (Kobulnicky & Koo 2000; Lemoine-Busserolle et al. 2002). Among these spectra is a rotation curve of a galaxy at  $z \sim 2$  that reaches a velocity of  $\gtrsim 200$   $\text{km s}^{-1}$  (Lemoine-Busserolle et al. 2002), suggesting that near-IR spectroscopy may be able to provide the most detailed kinematic information yet available on galaxies at high redshift. It is also clear from most of the above results that star formation rates measured from  $\text{H}\alpha$  are consistently higher than those measured from the UV continuum luminosity; this is in accordance with observations at  $z \sim 1$  (Glazebrook et al. 1999; Tresse et al. 2002) and at lower redshifts (e.g. Bell & Kennicutt 2001; also see Sullivan et al. (2000) and Buat et al. (2002) for comparisons of  $\text{H}\alpha$  and UV SFRs). The difference is generally accounted for by the differing sensitivities of the  $\text{H}\alpha$  and UV continuum star formation rate diagnostics to the presence of dust and to star formation history.

In this paper we present  $\text{H}\alpha$  spectroscopy in the  $K$ -band of 16 UV-selected galaxies in the redshift range  $2.0 < z < 2.6$ . In § 2 we describe our target selection process, observations, and data reductions. In § 3 we comment individually on any noteworthy features of the galaxies. § 4 addresses the kinematics of the galaxies: we discuss the rotation curves in § 4.1 and the one-dimensional velocity dispersions in § 4.2. In § 5 we calculate star formation rates from  $\text{H}\alpha$  and rest-frame UV emission and compare them, and we discuss our conclusions in § 6. We use a cosmology with  $H_0 = 70 \text{ km s}^{-1} \text{ Mpc}^{-1}$ ,  $\Omega_m = 0.3$ , and  $\Omega_\Lambda = 0.7$  throughout. In this cosmology, the universe at  $z = 2.3$  is 2.8 Gyr old, or 21% of its present age, and a proper distance of 8.2 kpc subtends an angular distance of  $1''$ .

## 2. TARGET SELECTION AND OBSERVATIONS

The objects discussed herein are drawn from a large sample of galaxies photometrically selected and spectroscopically confirmed to be in the redshift range  $2.0 \leq z \leq 2.6$ . We summarize the selection technique here; a more complete discussion will be given in a forthcoming paper. We have extended the broadband color criteria used to select galaxies at  $z \sim 3$  (Steidel & Hamilton 1993; Steidel, Pettini, & Hamilton 1995; Steidel et al. 1996) to other regions of the  $(U_n - G)$  vs.  $(G - \mathcal{R})$  plane, identifying candidates according to the following conditions:

$$\begin{aligned} G - \mathcal{R} &\geq -0.1 \\ U_n - G &\geq G - \mathcal{R} + 0.2 \\ G - \mathcal{R} &\leq 0.3(U_n - G) + 0.2 \\ U_n - G &< G - \mathcal{R} + 1.0 \end{aligned} \quad (1)$$

We refer to these objects as “BX” (e.g. Q1700-BX691); 92% of the objects satisfying these criteria are galaxies in the redshift range  $1.6 \leq z \leq 2.8$ , with 72% in the range  $2.0 \leq z \leq 2.6$ . These criteria were developed by calculating the colors that typical  $z \sim 3$  Lyman break galaxies (LBGs) would have if they were placed at  $z \sim 2$ ; they are therefore designed to select objects with similar intrinsic spectral energy distributions (SEDs) at both redshifts (Adelberger 2002). Our sample also contains

four “MD” objects (e.g. Q1623-MD107); these objects are detected in the  $U_n$ -band and meet the criteria

$$\begin{aligned} G - \mathcal{R} &< 1.2 \\ U_n - G &\leq G - \mathcal{R} + 1.5 \\ U_n - G &\geq G - \mathcal{R} + 1.0 \end{aligned} \quad (2)$$

They have the redshift distribution  $\langle z \rangle = 2.79 \pm 0.27$  (Steidel et al. 2003), so that the low redshift end of the distribution encompasses objects with  $z \leq 2.6$ . Both the BX and MD candidates are restricted to  $\mathcal{R} \leq 25.5$  (roughly equivalent to  $\mathcal{R} \lesssim 26$  at  $z \sim 3$ ). The two remaining objects in our sample, Q0201-B13 and CDFb-BN88, satisfy the BX criteria but have different names because they predated the systematic use of the  $z \sim 2$  selection technique. Once candidates are photometrically identified, we confirm their redshifts with rest-frame UV spectra obtained with the Low Resolution Imaging Spectrometer (LRIS; Oke et al. 1995) on the Keck I telescope. The redshifts from the UV interstellar absorption lines and  $\text{Ly}\alpha$  when present are listed in Table 1, and spectra for two of the objects are shown as examples in Figure 1. The rest-frame UV observations will be described in detail elsewhere.

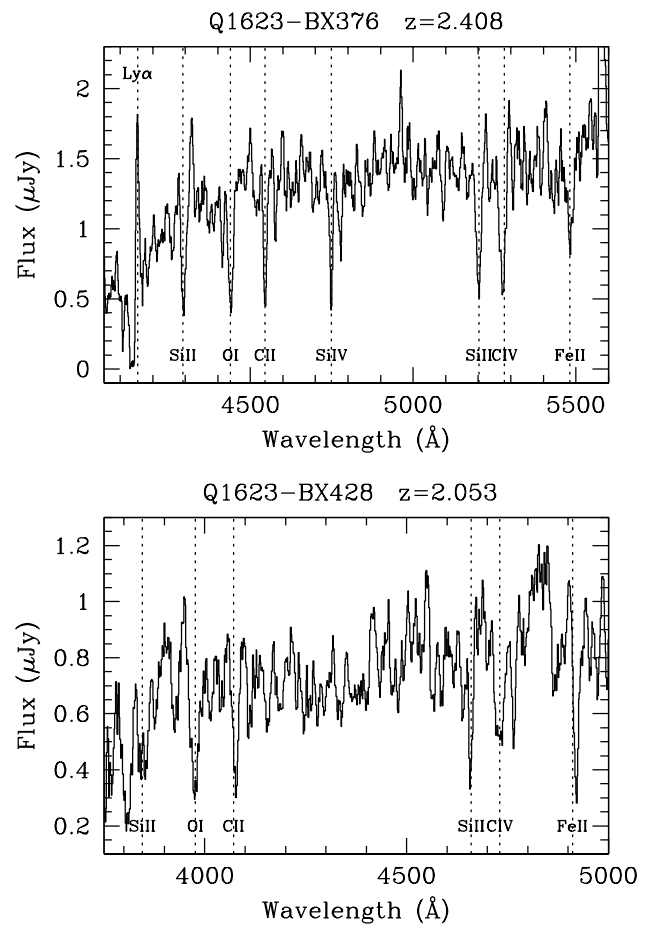


FIG. 1.— Sample rest frame UV spectra for two of the galaxies. We show Q1623-BX376 at  $z_{\text{abs}} = 2.408$  (top), and Q1623-BX428 at  $z_{\text{abs}} = 2.053$  (bottom). The rest wavelengths of the lines labeled are  $\text{Ly}\alpha \lambda 1215 \text{ \AA}$ ,  $\text{SiII} \lambda 1260 \text{ \AA}$ ,  $\text{OI} \lambda 1302 \text{ \AA}$ ,  $\text{CII} \lambda 1334 \text{ \AA}$ ,  $\text{SiIV} \lambda 1394 \text{ \AA}$ ,  $\text{SiII} \lambda 1526 \text{ \AA}$ ,  $\text{CIV} \lambda 1549 \text{ \AA}$ , and  $\text{FeII} \lambda 1608 \text{ \AA}$ .

The galaxies targeted for IR spectroscopy were selected as part of an ongoing project examining the interplay between

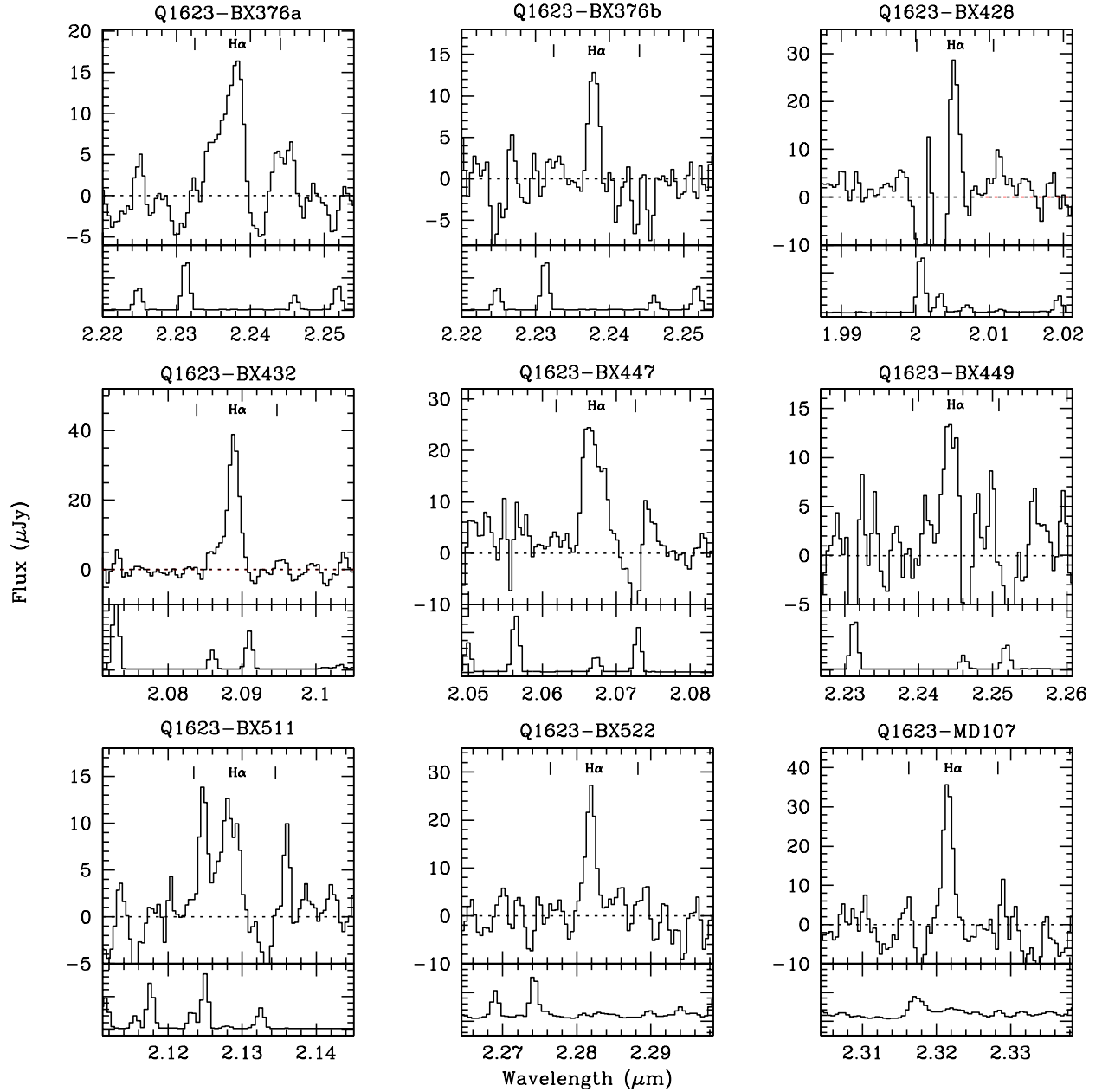


FIG. 2.— Fully reduced one-dimensional spectra for all of the galaxies in our sample. The  $\text{H}\alpha$  emission line is marked on each spectrum, and the vertical lines to either side mark the positions at which  $[\text{N II}]$  emission would appear. Plotted below each galaxy spectrum is a sky spectrum, in arbitrary flux units. The spectra have been smoothed with a two pixel boxcar filter. We discuss the objects individually in § 3.

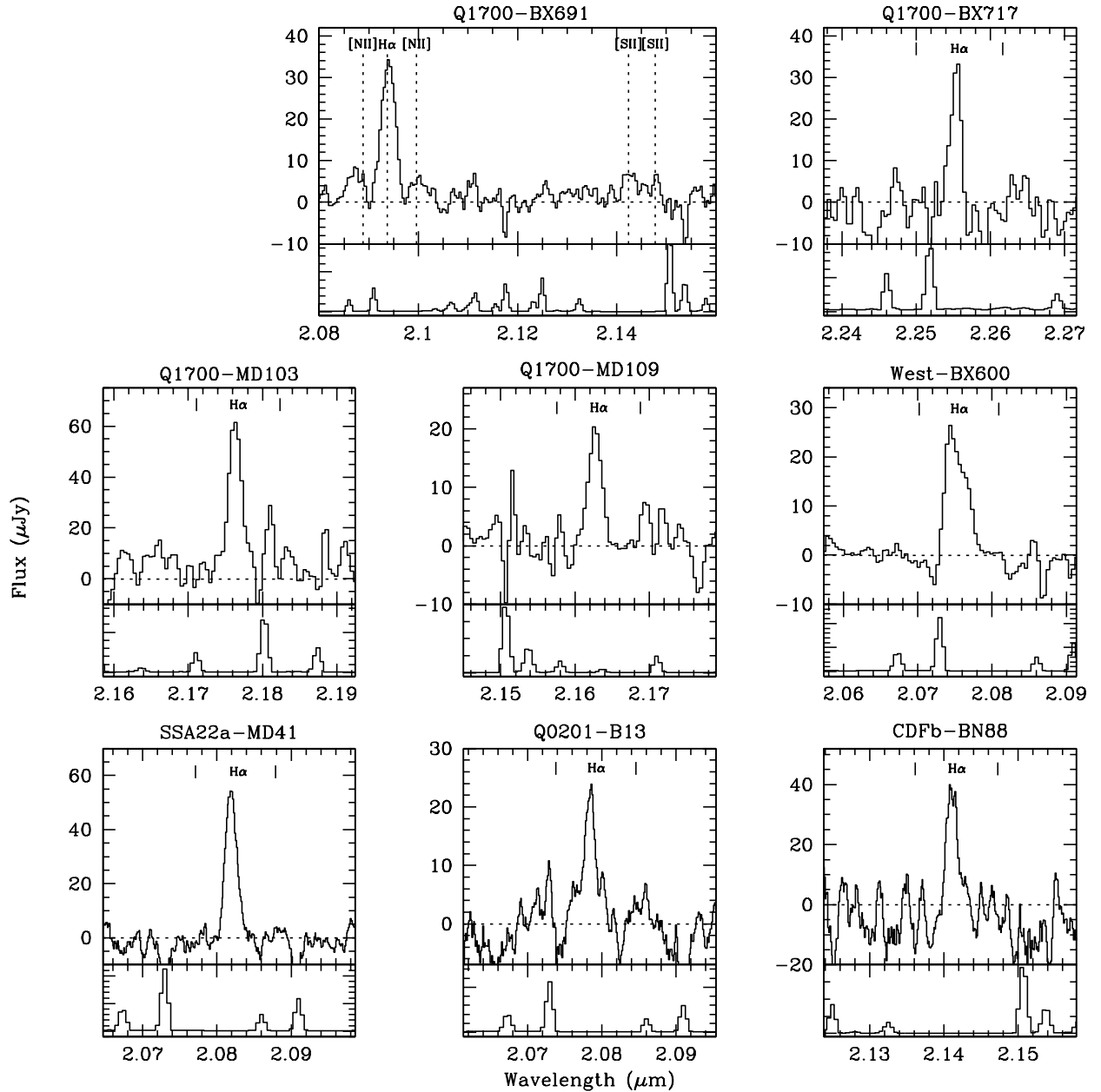


FIG. 2.— continued. We plot a larger wavelength range for Q1700-BX691, the only object in which we see [N II] and [S II] emission. The last three objects, SSA22a-MD41, Q0201-B13, and CDFb-BN88, were observed with ISAAC on the VLT, and their spectra have been smoothed to approximate the resolution of NIRSPEC.

galaxies and the intergalactic medium (IGM) in which we combine spectroscopy of faint star-forming galaxies with QSO absorption line observations of the IGM in the same volume (Adelberger et al. 2003). A detailed comparison of the galaxies and the IGM requires accurate measurements of the galaxy redshifts, and ultimately an understanding of the star formation rates, masses and ages of galaxies near the QSO lines of sight; therefore the primary selection criterion (beyond the color criteria described above) for the present sample was proximity to a QSO sight-line. This naturally results in a sample with a wide range of UV properties (as distinguished, for example, from the galaxies in the  $z \sim 3$  sample of Pettini et al. (2001), which were selected to be particularly UV-bright).

Twelve of our sixteen galaxies are within  $60''$  of QSOs in fields at  $1700+64$  and  $1623+27$ , and have redshifts slightly lower than those of the QSOs themselves; these were observed with the Near Infrared Imaging Spectrograph (NIRSPEC; McLean et al. 1998) on the Keck II telescope in May 2002. We observed an additional galaxy in the Groth-Westphal field on the same run. The other three objects in the sample (SSA22a-MD41, Q0201-B13, and CDFb-BN88) were observed with the Infrared Spectrometer and Array Camera (ISAAC; Moorwood et al. 1998) on the Very Large Telescope 1 (VLT 1) in October 2000, and were among the small number of  $z \sim 2-2.5$  galaxies in the  $z \sim 3$  LBG survey fields at the time. They were also selected because of their UV brightness, and because of the favorable wavelength of  $\text{H}\alpha$  relative to night sky emission lines and the possibility of measuring rotation.

### 2.1. Data Acquisition

Most of our targets were observed on May 19 and 20, 2002 (UT) with the NIRSPEC spectrograph on the Keck II telescope. NIRSPEC is described in detail by McLean et al. (1998); it uses a  $1024 \times 1024$  pixel (ALADDIN2) InSb detector with  $27 \mu\text{m}$  pixels. In the medium-dispersion mode used for these observations, each detector pixel corresponds to  $0.''143$  in the spatial direction, and the dispersion in the spectral direction is  $4.2 \text{ \AA}$  per pixel. We used a  $0.''76 \times 42''$  entrance slit, which gives a resolving power of  $R \simeq 1400$  corresponding to a spectral resolution of  $\sim 15 \text{ \AA}$  FWHM in the observed frame  $K$ -band, as measured from the widths of sky lines. In almost all cases we were able to place two galaxies on the slit at the same time by setting the appropriate position angle. Because the galaxies are too faint to be acquired directly on the spectrograph slit, we placed them on the slit by offsetting from a nearby bright star or from the QSO with a sight-line near the galaxy. Individual exposures were 900 s, and we typically took four exposures of each object for a total of 1 hour of integration. Between each exposure we reacquired the offset star, moved it along the slit by approximately  $5''$ , and offset once again to the target object. The detector was read out in multiple-read mode, with 16 reads at the start and end of each integration; the results were then averaged to reduce noise. The choice of filter and wavelength range was governed by the expected position of the  $\text{H}\alpha$  line based on each galaxy's optical redshift; we used the NIRSPEC6 and NIRSPEC7 filters, which span the wavelength ranges  $1.56-2.32$  and  $1.84-2.63 \mu\text{m}$  respectively. The spectral dispersion allows a range of approximately  $0.4 \mu\text{m}$  to be placed on the detector at one time. Conditions were photometric on both nights, with approximately  $0.''5$  FWHM seeing in  $K$ -band.

SSA22a-MD41, Q0201-B13, and CDFb-BN88 were ob-

served on October 20–22, 2000 (UT) with the ISAAC spectrograph on the VLT1. The short-wavelength channel of ISAAC (Moorwood et al. 1998) uses a  $1024 \times 1024$  pixel Rockwell HgCdTe array with  $18.5 \mu\text{m}$  pixels. The pixel scale along the  $1'' \times 120''$  slit is similar to that of NIRSPEC,  $0.''146 \text{ pixel}^{-1}$ , but the spectral resolution is 2.5 times higher, with  $R \simeq 3500$  and sky line widths of  $\sim 6 \text{ \AA}$  FWHM. We observed in the  $K$ -band, again targeting the expected position of  $\text{H}\alpha$  from rest-frame UV redshifts. The position angles were chosen to align with the major axes of the galaxies if any extended structure was apparent in the optical images; this was the case with SSA22a-MD41 and with CDFb-BN88 to a lesser extent. We also placed a bright star on the slit along with each galaxy to facilitate the determination of offsets between images. We performed an ABBA series of four 720 second exposures, with  $10''$  offsets between the A and B positions. The object was then reacquired at a different position along the slit and the procedure was repeated, typically for a total of  $\sim 3$  hours of integration. Conditions were not photometric, and the seeing varied between  $0.''5$  and  $0.''6$  FWHM. The targets and observations are summarized in Table 1.

### 2.2. Data Reduction

The fully reduced spectra are shown in Figure 2. The two-dimensional images were reduced with IRAF; preliminary steps included flagging and masking any pixels that exhibited aberrant behavior in the dark and flat-field images, flat-fielding the data using the spectrum of a quartz halogen lamp, and cutting out and rotating the image of the slit. Spatial distortion was corrected by stepping a bright star along the slit at  $5''$  intervals for the NIRSPEC data and  $10''$  intervals for that from ISAAC, combining the resulting images, and determining the star trace as a function of slit position. We then applied a wavelength solution to the rectified images by identifying the OH sky lines with reference to a list of vacuum wavelengths from the Kitt Peak National Observatory Fourier Transform Spectrograph<sup>4</sup>, resulting in 2-D images rectified both spatially and spectrally.

For the NIRSPEC objects, we took four 900 s exposures of each galaxy or galaxy pair, moving the object(s) along the slit for each integration. In order to subtract the sky background, we constructed a sky frame from the temporally adjacent images; after scaling and smoothing in the spatial direction, this sky frame was subtracted from the science image. Sky subtraction was done slightly differently for the ISAAC observations, which were taken using ABBA offsets: a sky frame made from the sum of the A images was subtracted from the B images, and vice versa. Further background subtraction was done for both the NIRSPEC and ISAAC observations by fitting a polynomial in the spatial direction at each wavelength bin, avoiding the positions of any bright objects on the slit; this removed some of the residuals of the sky lines. Finally, we produced a fully reduced, two-dimensional spectrogram of each galaxy by registering and averaging the individual frames, excluding bad pixels identified from combined dark and flat-field images. This step also produced a two-dimensional frame of the statistical  $1 \sigma$  error appropriate to each pixel. The last step was to extract one-dimensional spectra of each galaxy; this was done by summing the pixels containing a signal along the slit. The same aperture was then used to extract a variance spectrum from the square of the error image described above; the square root of this is a  $1 \sigma$  error spectrum which was used to determine the uncertainties in the line fluxes and widths.

<sup>4</sup>Available at <http://www.astro.caltech.edu/mirror/keck/inst/nirspec/data/oh.lst>

### 2.3. Flux Calibration

In order to put the one-dimensional spectra onto an absolute flux scale, we observed A0 and A2 stars from the list of UKIRT photometric standards<sup>5</sup>. These typically have  $K \simeq 7$  mag, and were observed at similar airmass and with the same instrumental configuration as the galaxies themselves. Flux calibration was done by scaling the spectral energy distribution of Vega (Colina, Bohlin, & Castelli 1996) according to the magnitude of the standard used, and dividing the spectrum of the standard star by this scaled Vega spectrum. This gives a sensitivity function in counts per unit flux density, by which we divided our one-dimensional galaxy spectra. Because the spectra of A stars are relatively smooth at the wavelengths of interest, they provide a measurement of the atmospheric absorption, and dividing our galaxy spectra by the sensitivity function therefore corrects for atmospheric absorption.

The uncertainties in the flux calibration process are both substantial and difficult to quantify; however, we have attempted to estimate them in several ways. As described above, we extracted  $1\sigma$  error spectra for each of the galaxies; these primarily reflect the noise of the sky background. By integrating the flux in the variance ( $\sigma^2$ ) spectrum at the position of  $\text{H}\alpha$  and taking the square root of the result, we can measure the random error associated with the observation; this is  $\leq 10\%$ . More difficult to measure are systematic errors: the largest sources of uncertainty are the flux lost due to imperfect centering of the objects on the slit, seeing and seeing variations, and the possibility of the objects being larger than the slit itself. We can get a sense of the importance of these effects by comparing the fluxes received in each of the individual exposures which were co-added to produce our final spectra. We find that flux levels between exposures vary by about 30% ( $1\sigma$ ); this includes random as well as systematic error. The uncertainty in the mean flux of our three or four exposures is then 15-20%. This accounts for variations in object centering and seeing, but not for flux consistently lost due to the width of the slit. As the galaxies observed are small ( $r_{1/2} \sim 0''.2$ - $0''.3$  in an *HST* WFPC2 pointing which includes several of them), we assume that in most cases the flux loss is not significant; however, a few of the galaxies are particularly irregular and extended, and in these cases the flux loss may be significant. We can perform a further check by calibrating the same object with several different standard stars; in doing so we find variations in flux of 15% at maximum, and usually much less (again,  $1\sigma$ ). Because we have  $K'$ -band photometry for one of the galaxies in our sample (Q1700-BX691, one of the few in which we detect a continuum signal), we can compare the photometric flux with the continuum flux; we find that our spectrum underestimates the photometric flux by a factor of 1.3, or about 25%. Because the continuum is so faint, this measurement is subject to large errors, and is more a test of our sky subtraction than of our spectrophotometry. We have also extracted one-dimensional spectra of the standard stars with a variety of aperture widths in order to determine whether an aperture correction might be necessary; we find that less than 5% of the flux is lost with the apertures used to extract the galaxy spectra. As this is much smaller than other sources of error, no aperture correction was applied. Based on all of these tests, we take our measured fluxes as uncertain by about 25%. This uncertainty propagates directly into the derived luminosities and star formation rates, and will be adopted in the analyses that follow.

### 3. COMMENTS ON INDIVIDUAL OBJECTS

While our selection process naturally leads to a wide range of UV properties, with  $\mathcal{R}$  ranging between 23.1 and 25.5 mag (i.e. a factor of 9 in luminosity), we see less variation in the  $\text{H}\alpha$  fluxes, which vary only by a factor of 4. The UV and  $\text{H}\alpha$  properties are not necessarily correlated, however; some of the strongest  $\text{H}\alpha$  luminosity comes from the faintest UV objects. Because we have rest-frame UV spectra of the galaxies, we are confident that none of them are AGN; we see no high-ionization emission lines, and few even show  $\text{Ly}\alpha$  emission. The lack of strong [N II] emission also indicates that the galaxies are not AGN. Veilleux & Osterbrock (1987) find that AGN have  $\log [\text{N II}] \lambda 6583 / \text{H}\alpha \gtrsim -0.2$ , while we detect [N II] emission in only one case, and that weakly. We hesitate to infer anything about the metallicity of the galaxies based on the absence of these lines, however, given the limited S/N of our data. The galaxies are faint, with no spectroscopically detected continuum in most cases, and we have not yet obtained rest-frame optical magnitudes; therefore we are unable to calculate  $\text{H}\alpha$  equivalent widths. We see a larger variation in the velocity dispersion  $\sigma$  than in previous samples of comparable size at high redshift (Pettini et al. 2001), but the most notable feature of our sample is the six galaxies which show evidence of ordered rotation, as we discuss in § 4.1. We comment on each object below.

*Q1623-BX376*: This is one of the brightest rest-frame UV objects in our sample, and the only one in which the star formation rate calculated from the UV emission is unambiguously higher than that from the  $\text{H}\alpha$  emission (see § 5). In ground-based imaging it appears extended, with a fainter component extending  $\sim 2''.5$  to the west. The association between the two components is less clear with higher-resolution imaging (see Figure 3); however, the  $\text{H}\alpha$  emission also consists of two lines at the same redshift, separated by  $2''.5$ . We have extracted spectra for both components, as shown in Figure 2; the primary component is labeled Q1623-BX376a, and the fainter Q1623-BX376b. Because our optical photometry treated both components as a single extended object, we sum the fluxes from both lines in order to calculate the  $\text{H}\alpha$  star formation rate in § 5.

*Q1623-BX428*: Unfortunately this galaxy lies at a redshift such that  $\text{H}\alpha$  falls very close to a strong sky line, to which we have lost significant flux. This can be seen clearly in Figure 2, where the sky line falls just to the left of  $\text{H}\alpha$ . Because of the loss of flux we are able to place a lower limit on the  $\text{H}\alpha$  star formation rate, but the sky subtraction has affected the line profile such that the velocity dispersion cannot be determined.

*Q1623-BX447*: This is one of the six galaxies for which we derived rotation curves from tilted  $\text{H}\alpha$  emission lines; it is also one of the few for which we have *HST* imaging, which shows it to be morphologically complicated (see Figure 3). We also see from the *HST* image that our slit was offset from the most extended axis of the galaxy by  $\sim 60$  degrees.

*Q1623-BX511*: Of the six galaxies for which we were able to derive rotation curves, this has the smallest  $\text{H}\alpha$  flux and hence the smallest spread in velocity and the largest uncertainties. The  $\text{H}\alpha$  emission falls between two bright sky lines, as can be seen in Figure 2. At  $\mathcal{R} = 25.37$  it is among the faintest UV objects in our sample as well.

*Q1700-BX691*: This is the only galaxy in which we clearly detect [N II]  $\lambda\lambda 6549, 6583$  and [S II]  $\lambda\lambda 6717, 6734$  emission lines as well as  $\text{H}\alpha$ . All of the lines are tilted in the two-dimensional spectra, providing strong evidence for rotation.

<sup>5</sup> Available at <http://www.jach.hawaii.edu/JACpublic/UKIRT/astronomy/calib/>

The  $\text{H}\alpha$  rotation curve reaches a velocity of  $\sim 240 \text{ km s}^{-1}$  at  $\sim 9 \text{ kpc}$ , with no sign of flattening; this is clearly a massive system. The fact that we see [N II] and [S II] lines suggests a relatively high metallicity; however, we defer a calculation until we are able to obtain measurements of [O III] in the  $H$ -band. Interestingly this is among the faintest UV objects in our sample, with  $\mathcal{R}=25.33$ . A  $K'$ -band image of this object (Teplitz et al. 1998; private communication) shows it to be extremely red, with  $\mathcal{R}-K'=5.10$ . The  $K'$ -band image also shows that our slit was fortuitously aligned with the major axis.

**Q1700-MD103:** This galaxy has the strongest  $\text{H}\alpha$  emission in our sample, and hence the largest  $\text{H}\alpha$ -derived star formation rate,  $27 \text{ M}_\odot \text{ yr}^{-1}$ . It is also one of the six objects in which we detect rotation.

**Westphal-BX600:** One of the six objects in which we detect rotation, this galaxy is second only to Q1700-BX691 in rotational velocity and implied mass. We detected  $\text{H}\alpha$  emission serendipitously, while observing the nearby  $z \sim 3$  galaxy Westphal-MD115. This object had been previously classified as a  $z \sim 2$  galaxy candidate based on its rest-frame UV colors, but it has not yet been observed with LRIS. Although we have no optical redshift, we believe the line detected here to be  $\text{H}\alpha$  because its UV colors are entirely consistent with a redshift of  $z = 2.16$ ; the contamination fraction in the optical color selection process is less than 10%, with most of the interlopers being galaxies at low redshift ( $z = 0.05$ – $0.15$ ). We do not know of any strong emission lines which would fall in our spectral window for a galaxy in this redshift range; for a redshift of  $z = 0.008$ ,  $\text{He I}$  ( $2.058 \mu\text{m}$ ; Lançon et al. 2001) would fall at the wavelength of the observed line, but then we would also expect to see stronger  $\text{Br}\gamma$  ( $2.166 \mu\text{m}$ ) emission at  $2.18 \mu\text{m}$ , which we do not.

**SSA22a-MD41:** This is one of the three galaxies which were observed with the ISAAC spectrograph on the VLT. Conditions were not photometric during the ISAAC run, so we are only able to place a lower limit on the  $\text{H}\alpha$  star formation rate. We detect rotation in the  $\text{H}\alpha$  emission, with a large spatial extent of nearly  $\pm 10 \text{ kpc}$ .

**Q0201-B13 and CDFb-BN88:** The other two galaxies observed with ISAAC. As with SSA22a-MD41, we place lower limits on the star formation rate from  $\text{H}\alpha$ . Q0201-B13 shows some evidence of rotation in a slight tilt of the emission line, but the signal-to-noise ratio (S/N) is too low to construct a reasonable rotation curve.

**Q1623-BX432, Q1623-BX449, Q1623-BX522, Q1623-MD107, Q1700-BX717, Q1700-MD109:** These are the remaining objects in the sample. They span a factor of three in  $\text{H}\alpha$  luminosity, from Q1623-BX432 at the bright end to Q1623-BX449 at the faint end, but none show evidence of velocity shear. Our only kinematic information about these objects comes from the velocity dispersion; for three of the fainter objects (Q1623-BX449, Q1623-MD107, and Q1700-BX717) we were only able to place an upper limit on this quantity.

**Non-detections:** There are 10 galaxies which we observed with NIRSPEC but failed to detect. Four of these are accounted for by two observations in which we did not detect either of the galaxies we placed on the slit; in the cases of the other six, we detected one of the galaxies on the slit, but missed the other. For one of these the optical redshift was unknown, so our hopes for detecting it were not high. These 10 non-detections could have a variety of explanations, including errors in our optical redshifts (which are of marginal quality in many cases), in the

astrometry, or in the guiding and tracking of the instrument and telescope. The objects could also be intrinsically faint due to extinction or a decline in the star formation rate, as discussed in § 5.

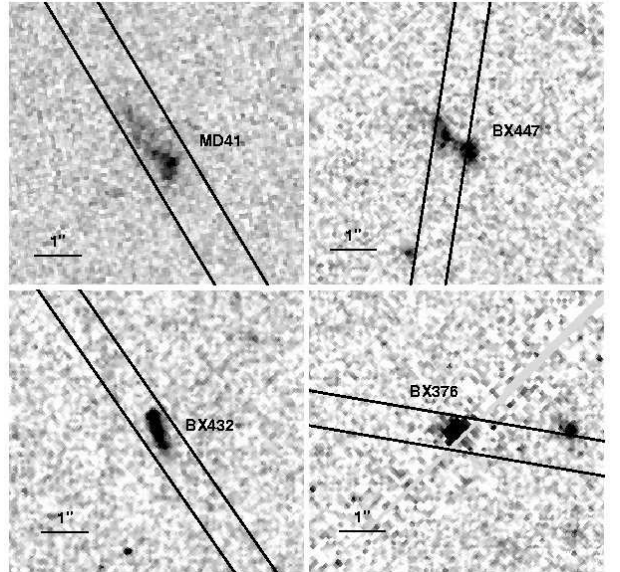


FIG. 3.— *HST* WFPC2 images of four of the galaxies in our sample. North is up and east to the left in all images, and positions of the slit are marked. *Upper left:* SSA22a-MD41, one of the objects in which we detect rotation, and the only one in which the slit was intentionally aligned with the major axis. *Upper right:* Q1623-BX447, another of the objects which show evidence of velocity shear. In this case the slit and the major axis were misaligned by  $\sim 60$  degrees. *Lower left:* We detect strong  $\text{H}\alpha$  emission from Q1623-BX432, but saw no evidence of velocity shear despite the near alignment of the slit along the major axis. *Lower right:* Q1623-BX376, the object with the largest velocity dispersion in our sample. We also detect  $\text{H}\alpha$  emission at the same redshift from the object on the right; the two were classified as one extended object in our ground-based photometry. The gray line running through the image is the boundary between two of the wide-field detectors.

#### 4. KINEMATICS

##### 4.1. Rotation

Six galaxies in our sample of 16 show evidence of velocity shear, in the form of a spatially resolved, tilted  $\text{H}\alpha$  emission line. We have constructed rotation curves for these objects by fitting a Gaussian profile in wavelength to the emission line at each spatial location along the slit, summing three pixels in the spatial direction at each point in order to approximate the seeing of  $\sim 0''.5$ . Velocity offsets were measured with respect to the systemic redshift of the galaxy as determined from the central wavelength of the integrated  $\text{H}\alpha$  emission line; when possible, the spatial center was defined by summing the spectra in the dispersion direction without including the emission line and locating the center of the continuum. For those with no apparent continuum emission (Q1700-MD103 and Q1623-BX511), the center was defined as the spatial center of the emission line. The 2-D emission lines are shown in Figure 4 and the rotation curves in Figure 5. The observed velocities range from  $\sim 50$  to  $\sim 240 \text{ km s}^{-1}$ , comparable to those observed in local galaxies and up to  $z \sim 1$  (Vogt et al. 1996, 1997). In most cases they show no sign of flattening at a terminal velocity; the blue-shifted end of the curve of West-BX600 is the only one that appears to flatten, and this is probably caused by imperfect subtraction of an adjacent sky line.

There are several systematic effects to be considered here;

most of them result in an underestimation of the rotational velocity. Except in the case of SSA22a-MD41, no attempt was made to align the slit with the major axis of the galaxy (position angles were chosen in order to place two objects on the slit; see § 2); in fact in most cases our ground-based images do not have sufficient resolution to allow the determination of a major axis. In the  $K'$ -band image of Q1700-BX691, however, it appears that here our slit was fortuitously aligned with the major axis of the galaxy. We also have an *HST* WFPC2 image of Q1623-BX447 (see Figure 3) in which it is apparent that the position angles of the slit and the galaxy differ by  $\sim 60$  degrees. In the other three cases, the slit and the major axis were misaligned by an unknown amount. In addition the inclinations of the galaxies are not known. Given a random inclination and a random slit orientation, we will on average underestimate the rotational velocity by a factor of  $(\pi/2)^2 \simeq 2.5$ , where a factor of  $\pi/2$  (the inverse of the average value of  $\sin x$  over the interval  $(0, \pi/2)$ ) comes from each effect. Also, because all or most of each galaxy falls within the slit, the velocity we measure at each spatial point along the slit is biased away from the maximum projected velocity at the major axis by the lower velocities of points away from the major axis. We must also consider the possibilities of uneven distribution of  $\text{H}\alpha$  emission and non-circular motions; both of these are likely, given the irregular morphologies of the galaxies (see Figure 3). A concentration of  $\text{H}\alpha$  away from the major axis of the galaxy would lead to an underestimate of the rotational velocity, but the effect of non-circular motions is more difficult to predict. Typically many of these effects are modeled and corrected for in rotation curves for less distant galaxies (Vogt et al. 1996, 1997; Swaters et al. 2002). Given the chaotic, or unknown, morphologies in our sample, we have not attempted to model these corrections.

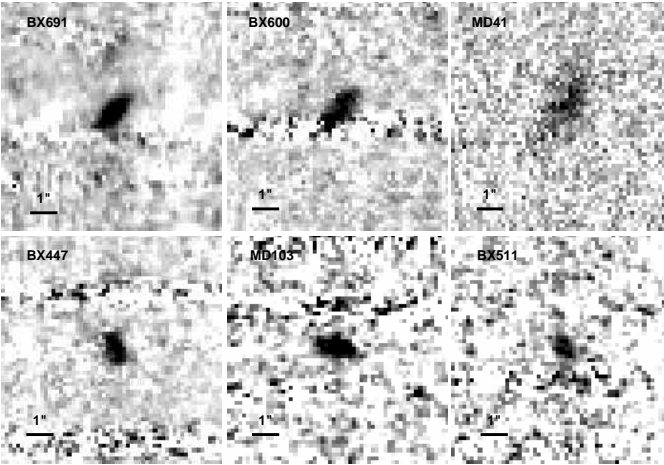


FIG. 4.— The two-dimensional spectra of the galaxies for which we have derived rotation curves, showing the tilt in the  $\text{H}\alpha$  emission line. From upper left, the galaxies are Q1700-BX691 at  $z = 2.1895$ ; West-BX600 at  $z = 2.1607$ ; SSA22a-MD41 at  $z = 2.1713$ ; Q1623-BX447 at  $z = 2.1481$ ; Q1700-MD103 at  $z = 2.3148$ ; and Q1623-BX511 at  $z = 2.2421$ . A tilted  $[\text{N II}]\lambda 6584$  emission line is visible above  $\text{H}\alpha$  in the spectrum of Q1700-BX691. The  $x$  axis is spatial, with  $1''$  scale bars shown, and  $y$  is the dispersion direction.

We have used archival *HST* WFPC2 images that contain two of these galaxies, SSA22a-MD41 (in the F814W filter; proposal ID 5996) and Q1623-BX447 (F702W; proposal ID 6557). We reduced the images following the drizzling procedure outlined in the *HST* Dither Handbook (Koekemoer et al. 2002); see Fruchter & Hook (2002) for more details. The images are shown in Figure 3, with the position of the slit marked. Nei-

ther appears to be a well-formed disk; most of the rest-frame UV emission in SSA22a-MD41 is concentrated in a knot at the southwest edge, and Q1623-BX447 shows two distinct areas of emission. It is interesting to contrast these with images of two other galaxies for which we did not detect rotation: Figure 3 also shows images of Q1623-BX432 and Q1623-BX376, which are also contained in the Q1623 pointing and which also appear irregular. This demonstrates the difficulty of predicting the kinematics of these objects from even high-resolution imaging; complicated morphologies make inclinations and major axes difficult to determine, and objects with similar UV continuum morphologies may exhibit quite different  $\text{H}\alpha$  kinematic properties. We also point out that the  $\text{H}\alpha$  and UV emission may not be coincident; Pettini et al. (2001) observed nebular line emission extending  $\sim 1''$  beyond the UV emission in a galaxy at  $z = 3.2$ , and similar effects have been seen in local galaxies (Leitherer et al. 1996; de Mello et al. 1998; Johnson et al. 2000). Specifically, Conselice et al. (2000) compared  $\text{H}\alpha$  and UV emission in six nearby starburst galaxies, finding that the  $\text{H}\alpha$  and UV fluxes were well correlated in three of the systems, but that they showed different morphologies in the other three.

Although we have no direct evidence that these galaxies are in fact disks, we make this assumption in order to use the radius  $r$  and the circular velocity  $v_c$  to calculate the enclosed mass,

$$M_{\text{dyn}} = v_c^2 r / G. \quad (3)$$

Since we have neither well-defined terminal velocities nor spatial centers for these objects, we have calculated lower limits on the masses by using half of the total spread in both velocity and distance, for  $v_c$  and  $r$  respectively. We obtain an average dynamical mass of  $\langle M \rangle \geq 4 \times 10^{10} \text{ M}_\odot$ ; individual masses for each galaxy are shown in Table 2. As the  $\text{H}\alpha$  emission traces only the central star-forming regions of these objects, which are probably baryon-dominated, the masses derived are underestimates of the total halo masses of the galaxies. We can use an order of magnitude argument to estimate the total masses: for  $\Omega_b = 0.02h^{-2}$  and  $\Omega_m = 0.3$ ,  $\Omega_m/\Omega_b \sim 7$ , and the universe contains about six times more dark than baryonic matter. We therefore expect the total masses of the galaxies to be about seven times larger than their stellar masses, and we place a lower limit of  $M \gtrsim 3 \times 10^{11} \text{ M}_\odot$  on the typical halo mass of these galaxies. This is generally consistent with mass estimates from the clustering properties of LBGs at  $z \sim 3$ : Adelberger et al. (1998) find a typical mass of  $8 \times 10^{11} h^{-1} \text{ M}_\odot$  for a  $\Lambda$ CDM model, based on the number density and correlation length of the galaxies. Other analyses yield similar results (Baugh et al. 1998; Giavalisco & Dickinson 2001). We defer an analysis of the clustering of the  $z \sim 2$  galaxies to a later work. We can also compare our mean baryonic mass with the median stellar mass from population synthesis models found for LBGs at  $z \sim 3$  by Shapley et al. (2001),  $m_{\text{star}} = 1.2 \times 10^{10} h^{-2} \text{ M}_\odot$ ; again the two are in rough agreement.

There are few other examples of such rotation curves at redshifts of  $z \gg 1$ . Lemoine-Busserolle et al. (2002) have recently reported a rotation curve of a gravitationally lensed galaxy at  $z = 1.9$ ; the rotation curve looks much like those we present here, with  $v \gtrsim 200 \text{ km s}^{-1}$  at a radius of  $\sim 1''$ , although when the lensing correction is applied this radius corresponds to only  $\sim 1 \text{ kpc}$ . Genzel et al. (2002) have used millimeter interferometry to observe rest-frame  $335 \mu\text{m}$  continuum and  $\text{CO}(3-2)$  line emission from a massive submillimeter galaxy at  $z = 2.8$ ; their data indicate a rotating disk with velocity  $\geq 420 \text{ km s}^{-1}$  at  $\sim 8 \text{ kpc}$  in radius. From observations of  $[\text{O III}]$  at  $z \simeq 3.2$ , Moor-

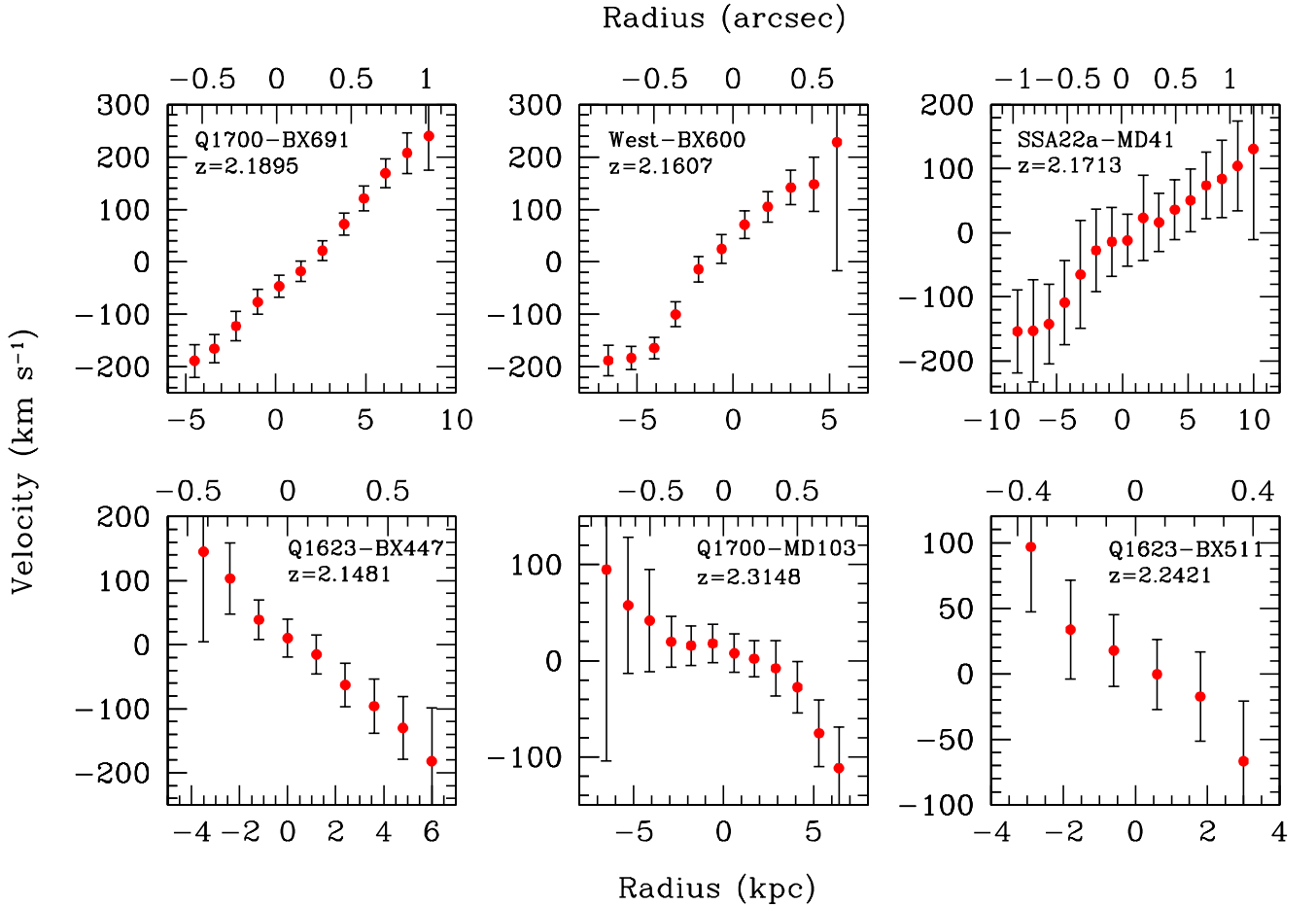


FIG. 5.—Rotation curves for the six galaxies that show spatially resolved, tilted H $\alpha$  emission lines. From the rotational velocities and radii we derive lower limits on the mass of each galaxy; the mean dynamical mass is  $\langle M_{dyn} \rangle \geq 4 \times 10^{10} M_{\odot}$ . The galaxies are shown in order of decreasing mass; from upper left, Q1700-BX691, West-BX600, SSA22a-MD41, Q1623-BX447, Q1700-MD103, and Q1623-BX511. Note that the points are correlated due to the seeing of  $\sim 0.5''$ . We have used a cosmology with  $H_0 = 70 \text{ km s}^{-1} \text{ Mpc}^{-1}$ ,  $\Omega_m = 0.3$ , and  $\Omega_{\Lambda} = 0.7$  for the transformations between arcsec and kpc.

wood et al. (2003) present a rotation curve with a velocity of  $108 \text{ km s}^{-1}$  at  $\simeq 12 \text{ kpc}$ . Also in observations of [O III] and H $\beta$  in 15 LBGs at  $z \sim 3$ , Pettini et al. (2001) see two spatially resolved and tilted emission lines, but the observed velocities reach only  $\sim 50 \text{ km s}^{-1}$ . Simply counting the instances of rotation shows that the two samples are different at the 95% confidence level; the difference is actually more significant, because this test does not account for the larger rotational velocities at  $z \sim 2$ . It is interesting that we see stronger evidence for rotation in a sample of similar size at  $z \sim 2$ , and we will spend a moment speculating on the possible reasons for this. Poorer seeing during the  $z \sim 3$  observations could perhaps account for the differences; this does not explain the larger values of the velocity dispersion  $\sigma$  we see at  $z \sim 2$  (see § 4.2), however, as these should be unaffected even if the lines are spatially unresolved. It might then be that H $\alpha$  is a more sensitive probe of rotation and velocity dispersion than [O III] because of higher surface brightness; but Pettini et al. (2001) typically measured  $[\text{O III}]\lambda 5007/\text{H}\beta \sim 3$ , and H $\alpha/\text{H}\beta \sim 3$  as well, so H $\alpha$  and  $[\text{O III}]\lambda 5007$  should have roughly comparable strengths in the  $z \sim 3$  galaxies. We also note that in rotation curves for which they had both H $\alpha$  and  $[\text{O III}]\lambda 5007$  data, Vogt et al. (1996) found that the flux distributions and velocities of the two lines matched well. Lemoine-Busserolle et al. (2002) also have both H $\alpha$  and  $[\text{O III}]\lambda 5007$  observations for their rotation curve, and again the two lines give comparable results. The differences could also be due to S/N effects; but the  $z \sim 3$  galaxies were generally observed with longer integration times than those in the current sample, and their spectra have S/N comparable to or higher than that of those presented here. We should also discuss the possibility that we may be observing different populations of galaxies at  $z \sim 2$  and  $z \sim 3$ . We therefore consider the evidence for other intrinsic differences between galaxies at the two redshifts. The most obvious of these is apparent UV luminosity; the galaxies of Pettini et al. (2001) are brighter than those presented here, with only a few exceptions. This is simply because the brightest galaxies were selected for IR observation at  $z \sim 3$ , but not at  $z \sim 2$ . As discussed in § 2, however, the  $z \sim 2$  selection criteria were chosen so that the galaxies they select would have SEDs similar to galaxies at  $z \sim 3$ . If we are indeed looking at different sets of objects at  $z \sim 2$  and  $z \sim 3$ , both the average and range of their far-UV properties must be similar (although we do sample the luminosity function more deeply at  $z \sim 2$ ). It is also possible that we are observing the two samples to different radii: surface brightness is a strong function of redshift, scaling as  $(1+z)^4$ , and this may limit the radii to which we can observe the galaxies at higher redshift. Star formation progressing to larger radii in the disks at later times could produce a similar effect. It is also possible that our stronger evidence for rotation reflects an increase in the number of rotating galaxies and their rotational speeds between  $z \sim 3$  and  $z \sim 2$ . With the present data such a conclusion would be premature, however, since we cannot rule out all observational effects.

It is interesting to consider objects such as these in the context of hierarchical models of galaxy formation. We compare our data with predictions of the properties of LBGs at  $z \sim 3$  (Mo, Mao, & White 1998, 1999), although it is not yet clear how the current sample and the  $z \sim 3$  galaxies are related. LBGs are thought to be the central galaxies of the most massive dark halos present at  $z \sim 3$ , and they are predicted to be small and

to have moderately high halo circular velocities but low stellar velocity dispersions. For a  $\Lambda$ CDM cosmology, Mo et al. (1999) predict that the median effective radius  $R_{\text{eff}}$  (defined as the semimajor axis of the isophote containing half of the star formation activity) is about  $2 \text{ h}^{-1} \text{ kpc}$ , and most galaxies should have  $R_{\text{eff}}$  between 0.8 and  $5 \text{ h}^{-1} \text{ kpc}$ . While the maximum radial extent of some of our rotation curves is larger than this, it is likely that the galaxies are visible at radii beyond  $R_{\text{eff}}$ , and these predictions are consistent with our measurements of half-light radii from the WFPC2 images. Mo et al. (1999) also predict a median halo circular velocity of  $290 \text{ km s}^{-1}$  for  $\Lambda$ CDM, with most galaxies falling between  $220$  and  $400 \text{ km s}^{-1}$ , and a median stellar velocity dispersion of  $\sim 120 \text{ km s}^{-1}$ . Both of these predictions are reasonably consistent with our data, considering that we have not corrected our circular velocities for inclination or slit alignment effects, and that our velocities are lower limits due to the lack of flattening in the rotation curves. In fact, as noted above, the  $z \sim 2$  galaxies are a better match to these predictions than the  $z \sim 3$  LBGs, which have observed rotational velocities of only  $\sim 50$ – $100 \text{ km s}^{-1}$  and velocity dispersions of  $\sim 70 \text{ km s}^{-1}$ .

Finally, additional observations will clarify the kinematics of the  $z \sim 2$  sample. High resolution imaging in both the optical and the IR will allow a determination of the morphologies of the galaxies and the extent of the rest-frame optical emission; spectroscopic observations with varying position angles will provide strong constraints on rotating disk models. We are also optimistic about the possibility of obtaining a larger sample of rotation curves, since those presented here represent almost 40% of the galaxies observed. Looking farther into the future, integral field IR spectrographs that provide kinematic information at high spatial resolution over a contiguous region encompassing the entire galaxy will be ideal for probing the dynamics of high redshift galaxies; this may be the only way that the kinematic major axes of these objects can be determined.

## 4.2. Velocity Dispersions

We can obtain a limited amount of information about the dynamics and masses of the galaxies by simply measuring the widths of the emission lines. We have measured the one-dimensional velocity dispersion  $\sigma$  by fitting a Gaussian profile to each emission line, measuring its FWHM, and subtracting the instrumental broadening in quadrature from the FWHM. The instrumental broadening was measured from the widths of sky lines, and is  $\sim 15 \text{ \AA}$  for NIRSPEC and  $\sim 6 \text{ \AA}$  for ISAAC. The velocity dispersion is then the corrected FWHM divided by 2.355. We find a mean velocity dispersion of  $\langle \sigma \rangle \sim 110 \text{ km s}^{-1}$ , with a maximum of  $260 \text{ km s}^{-1}$ . The dispersions for each galaxy are shown in Table 2, with  $1 \Delta_{\sigma}$  uncertainties from propagating the errors in each Gaussian fit (to avoid confusion stemming from overuse of the symbol  $\sigma$ , we use  $\Delta_{\sigma}$  to represent the standard deviation in the velocity dispersion). Most of the lines are resolved; for those that are not we have set an upper limit of  $2 \Delta_{\sigma}$ . Our average velocity dispersion is  $\sim 60\%$  higher than that found from the widths of  $[\text{O III}]\lambda 5007$  and H $\beta$  at  $z \sim 3$  by Pettini et al. (2001), who found a median of  $\sim 70 \text{ km s}^{-1}$ .<sup>6</sup>

Assuming that these velocities are due to motion of the gas in the gravitational potential of the galaxy, we can estimate the masses of the galaxies. For the simplified case of a uniform

<sup>6</sup>We also find a mean of  $\sim 70 \text{ km s}^{-1}$  in the  $[\text{O III}]\lambda 5007$  velocity dispersions of a sample of 11 LBGs at  $z \sim 3$  which we observed with NIRSPEC in April 2001. These data are unpublished, and will be described in detail in a later work.

sphere,

$$M_{vir} = 5\sigma^2(r_{1/2}/G). \quad (4)$$

From the *HST* image of the galaxies in the Q1623 field, we find  $r_{1/2} \sim 0.^{\prime\prime}2$ , which in our adopted cosmology corresponds to  $\sim 1.6$  kpc at  $z = 2.3$ . We use this value to calculate the masses shown in Table 2. Accounting for the lower limits on four of the objects by using ASURV Rev. 1.2 (Lavalley, Isobe, & Feigelson 1992), a software package which calculates the statistical properties of samples containing limits or non-detections (survival analysis; Feigelson & Nelson 1985), we find a mean mass of  $\sim 2 \times 10^{10} M_{\odot}$ ; this is in general agreement with the rotationally-derived masses in § 4.1. As we noted when deriving masses from the rotation curves above, because the nebular emission comes mostly from the central star-forming regions of high-surface brightness, the velocity dispersions probably do not reflect the full gravitational potential of the galaxies.

There are several issues to consider in the interpretation of these mass estimates. In addition to the obvious caveats related to the assumption of spherical geometry, the uncertain value of  $r_{1/2}$ , and the sometimes large uncertainties in  $\sigma$ , we should consider whether or not the line broadening is indeed gravitational in origin. Galaxy-scale starburst-driven outflows with speeds of several hundred  $\text{km s}^{-1}$  have been shown to be ubiquitous in star-forming galaxies at  $z \sim 3$  (Pettini et al. 2001). These are measured from the offsets of  $\text{Ly}\alpha$  and the interstellar absorption lines with respect to the systemic velocity of the galaxy;  $\text{Ly}\alpha$  is consistently redshifted with respect to the systemic velocity, while the interstellar lines are blueshifted. We are unable to determine conclusively whether or not similar outflows exist in the present sample, since in many cases the S/N ratios of our rest-frame UV spectra are too low to determine redshifts from  $\text{Ly}\alpha$  and interstellar absorption lines with the necessary precision. However, for those objects that have spectra of sufficient quality, we have measured the velocities of the interstellar absorption lines and  $\text{Ly}\alpha$  with respect to the  $\text{H}\alpha$  redshifts. The results are shown in Figure 6. We see that in this small sample,  $\text{Ly}\alpha$  is consistently redshifted by several hundred  $\text{km s}^{-1}$ , but that the interstellar lines are both blueshifted and redshifted with respect to  $\text{H}\alpha$ . This offers marginal support for the existence of outflows, but clearly a larger sample is necessary. Even if these outflows do exist, however, it is not clear that they would result in an increase in the velocity dispersion. Our velocity dispersions are from  $\text{H}\alpha$  emission, which we take to be coming primarily from nebular gas at the systemic redshift of the galaxy, not from outflowing material. In addition, a correlation between the velocity dispersion and the speed of the outflow (here defined as the average of  $v_{\text{Ly}\alpha} - v_{\text{neb}}$  and  $v_{\text{neb}} - v_{\text{IS}}$ ) might be expected if the line broadening were due to outflowing gas. With this in mind we have examined a sample of 23 galaxies at  $z \sim 3$  for which we have both velocity dispersions from the width of the  $[\text{O III}]\lambda 5007$  emission line and outflow velocities from the offsets between the nebular, interstellar absorption and  $\text{Ly}\alpha$  redshifts. We see no evidence for a strong link between the velocity dispersion and the speed of the outflow; the correlation coefficient between them is 0.13. These considerations lead us to believe that the presence of outflows is not a strong argument against gravitational broadening of the lines.

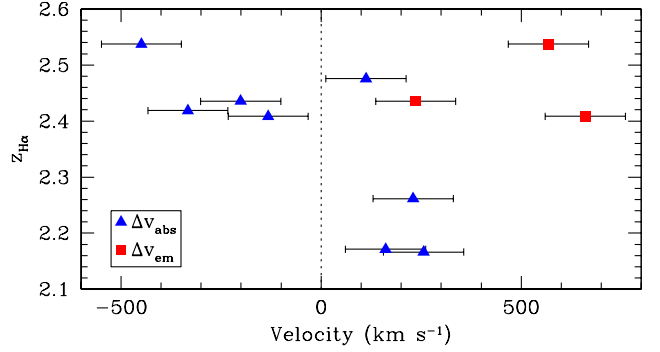


FIG. 6.— Velocity offsets between the systemic velocity of  $\text{H}\alpha$  and the velocities of the interstellar absorption lines (blue triangles) and  $\text{Ly}\alpha$  emission (red squares). The sample is small because most of our galaxies do not have rest-frame UV spectra of sufficient S/N to make this comparison.

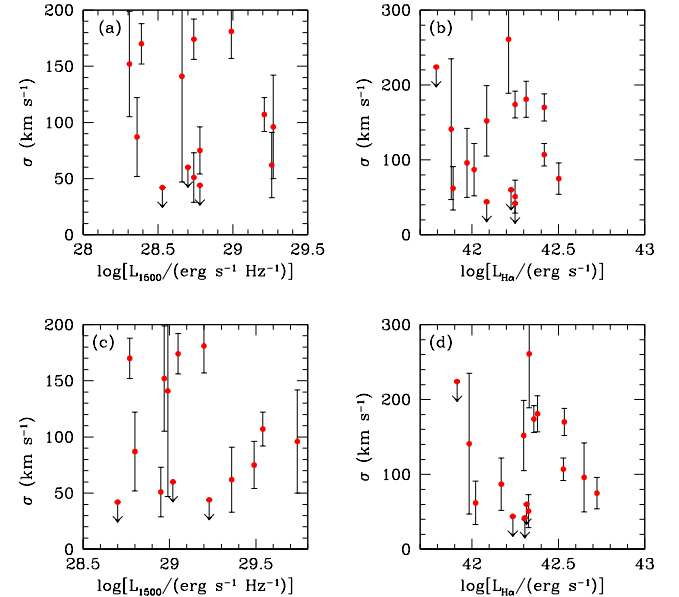


FIG. 7.— The velocity dispersion  $\sigma$  plotted against the 1500  $\text{\AA}$  continuum and  $\text{H}\alpha$  luminosities, without extinction corrections (a and b), and corrected as described in the text (c and d). Arrows indicate upper limits on  $\sigma$ . See § 5 for a discussion of the errors in luminosity.

We are also struck by the spatial complexity of some of these objects. In particular, the  $\text{H}\alpha$  emission of Q1623-BX376 appears as two lines at the same redshift but separated by  $2.^{\prime\prime}5$ . The brighter of these, Q1623-BX376a, has the largest velocity dispersion in the sample, and shows an asymmetric line profile (see Figure 2), with a blue-shifted tail extending about  $0.^{\prime\prime}5$  in the opposite direction from the fainter component, Q1623-BX376b. It is primarily this tail which is responsible for the large velocity dispersion. This faint emission is also visible in the WFPC2 image shown in Figure 3 (where, unfortunately, the galaxy falls on the border between two of the wide-field detectors). Given the complicated structure of this object, we hesitate to attribute its broad emission line purely to random gravitational motions; galactic mergers or interactions could also produce such broadened emission lines and disturbed morphologies.

As a final test, we compare the one-dimensional velocity dis-

dispersion with luminosity. We see from Figure 7 that neither the 1500 Å continuum nor the H $\alpha$  emission line luminosity correlate with velocity dispersion, either with or without a correction for extinction. Such a lack of correlation is also seen for galaxies at  $z \sim 3$  (Pettini et al. 2001). This does not necessarily mean that the line widths are unrelated to the masses of the galaxies; it may be that large variations in the mass-to-light ratio are blurring any trend. We conclude that while these caveats are important, none of them provide a compelling argument against using the velocity dispersions to estimate the masses of the galaxies; therefore for the moment we will continue to do so.

##### 5. STAR FORMATION RATES AND EXTINCTION

H $\alpha$  emission is one of the primary diagnostics of the star formation rate (SFR) in local galaxies, and therefore its observation at high redshift is particularly valuable for the sake of comparison with nearby samples. Redshifts of  $z \lesssim 2.6$  are the highest at which H $\alpha$  can currently be detected before it shifts out of the near-IR  $K$ -band window. Except for a few other observations of H $\alpha$  at  $z > 2$  (Teplitz et al. 1998; Kobulnicky & Koo 2000), most determinations of the star formation rate at high redshift have so far been based on the UV stellar continuum and, to a lesser extent, the H $\beta$  emission line (Pettini et al. 2001). Here we compare star formation rates for the 16 galaxies in our sample deduced from the H $\alpha$  flux and from the UV continuum emission; as the two are affected differently by dust and star formation history, our results can in principle tell us about the extinction and stellar populations of the galaxies. We have calculated H $\alpha$  SFRs following Kennicutt (1998):

$$\text{SFR} (M_{\odot} \text{ yr}^{-1}) = 7.9 \times 10^{-42} L(\text{H}\alpha) (\text{erg s}^{-1}) \quad (5)$$

The nebular recombination lines are a direct probe of the young, massive stellar population, since only the most massive and short-lived stars ( $M \gtrsim 10 M_{\odot}$ ) contribute significantly to the ionizing flux. Thus the emission lines provide a nearly instantaneous measure of the SFR, independent of the star formation history. The above equation assumes a Salpeter IMF with upper and lower mass cutoffs of 0.1 and 100  $M_{\odot}$  and case B recombination at  $T_e = 10,000$  K. It also assumes that all of the ionizing photons are reprocessed into nebular lines, i.e. that they are not absorbed by dust before they can ionize an atom, and that they do not escape the galaxy.

Ultraviolet-derived star formation rates were calculated from the broadband optical photometry, using the  $G$  magnitude as an approximation for the 1500 Å continuum (at  $z = 2.3$ , the mean redshift of our sample, the central wavelength of the  $G$  filter, 4830 Å, falls at a rest wavelength of 1464 Å). SFRs were calculated as follows (Kennicutt 1998):

$$\text{SFR} (M_{\odot} \text{ yr}^{-1}) = 1.4 \times 10^{-28} L_{1500} (\text{erg s}^{-1} \text{ Hz}^{-1}) \quad (6)$$

This relationship applies to galaxies with continuous star formation over time scales of  $10^8$  years or longer; for a younger population, the UV continuum luminosity is still increasing as the number of massive stars increases, and the above equation will underestimate the star formation rate. The assumed IMF is the same as above.

The fluxes and corresponding SFRs are summarized in Table 3, and a comparison of the uncorrected star formation rates is shown in the left panel of Figure 8. The error bars reflect

the uncertainties in flux calibration of the H $\alpha$  emission and the UV photometry, about 25% and 10% respectively; for the H $\alpha$  spectra this includes both random and systematic error, as discussed in § 2.3, and is likely an underestimate in the noisiest cases. Uncertainties in the conversion from flux to SFR are not included. There are four objects for which we are only able to place lower limits on the SFR from H $\alpha$ : Q1623-BX428, in which the H $\alpha$  line fell on top of a strong sky line to which we have lost significant flux, and SSA22a-MD41, Q0201-B13, and CDFb-BN88, which were observed during non-photometric conditions (and calibrated with the least extinguished exposure of a standard, in order to place lower limits). Without correcting for extinction, we find  $\text{SFR}_{\text{H}\alpha} > \text{SFR}_{\text{UV}}$  in all but five cases; four of these are the lower limits described above. We find  $\langle \text{SFR}_{\text{H}\alpha}/\text{SFR}_{\text{UV}} \rangle = 2.4$ ; this was computed using ASURV Rev. 1.2 (Lavallee, Isobe, & Feigelson 1992), a software package which calculates the statistical properties of samples containing limits or non-detections (survival analysis; Feigelson & Nelson 1985). This result is in qualitative agreement with previous observations of galaxies at  $z \gtrsim 1$ : Yan et al. (1999) find that the global star formation rate derived from H $\alpha$  exceeds that from the UV by a factor of  $\sim 3$ , and Hopkins et al. (2000) obtain a measurement of SFR density from H $\alpha$  at  $0.7 \leq z \leq 1.8$  that is a factor of 2–3 greater than that estimated from UV data. Glazebrook et al. (1999) study a sample of 13 galaxies at  $z \sim 1$  from the Canada France Redshift Survey (CFRS); when the same Kennicutt (1998) calibrations are used, their data give an H $\alpha$  SFR 1.9 times higher than the UV SFR, without applying an extinction correction (Yan et al. 1999).<sup>7</sup> It is also comparable to the results of Bell & Kennicutt (2001), who find  $\langle \text{SFR}_{\text{H}\alpha}/\text{SFR}_{\text{UV}} \rangle = 1.5$  for galaxies with  $\text{SFR} \gtrsim 1 M_{\odot} \text{ yr}^{-1}$  in a sample of 50 nearby star-forming galaxies. There is clearly a trend for the H $\alpha$ -derived SFRs to be higher than those from the UV luminosity, in spite of differing selection criteria; both the Yan et al. (1999) and Hopkins et al. (2000) samples were selected in the IR, while ours is UV-selected and the Bell & Kennicutt (2001) sample is drawn from local galaxies observed by the Ultraviolet Imaging Telescope (UIT). We will discuss possible reasons for this trend below. We also note that the one remaining object with a larger UV SFR, Q1623-BX376, is a somewhat unusual case. It is bright and extended in the UV, and the H $\alpha$  emission appears in two distinct lines at the same redshift but separated by 2''.5. Since the UV photometry encompassed both components we have added the flux from both lines to calculate the H $\alpha$  SFR, but it is clear from the WFPC2 image of Q1623-BX376 (Figure 3) that the fainter of the two components is largely off the edge of the slit; therefore we have likely missed some of the H $\alpha$  emission.

<sup>7</sup>Yan et al. (1999) and Glazebrook et al. (1999) assume  $H_0 = 50 \text{ km s}^{-1} \text{ Mpc}^{-1}$  and  $q_0 = 0.5$ . Using this cosmology lowers our SFRs by 5–10%; the ratios of the H $\alpha$  and UV rates are, of course, unaffected.

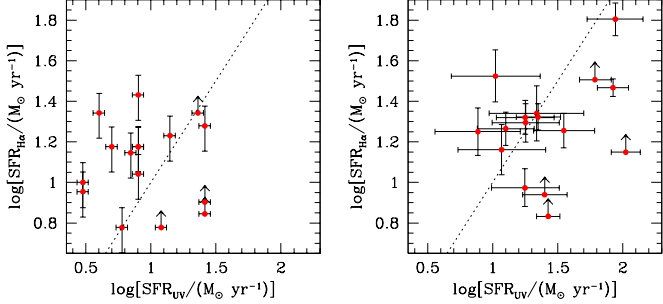


FIG. 8.— *Left:* Star formation rates from  $\text{H}\alpha$  and UV emission, uncorrected for extinction. Arrows indicate lower limits on the  $\text{H}\alpha$  SFR for objects observed during non-photometric conditions (SSA22a-MD41, Q0201-B13, and CDFb-BN88) or contaminated by sky lines (Q1623-BX428). Errors are 25% in  $\text{SFR}_{\text{H}\alpha}$  and 10% in  $\text{SFR}_{\text{UV}}$ , reflecting uncertainties in flux calibration. Uncertainties in the conversion from flux to SFR are not included. *Right:* The SFRs corrected for extinction as described in § 5. The error bars reflect uncertainties in  $E(B-V)$  only; flux calibration errors and errors in conversion from flux to SFR are not included. The dotted lines represent equal rates from  $\text{H}\alpha$  and UV emission.

There are at least two possible explanations for the larger  $\text{H}\alpha$  SFRs: dust extinction and the two star formation rate indicators' differing sensitivities to the ages of stellar populations and star formation histories. Our observations are consistent with the assumption that the ultraviolet emission generally suffers greater extinction than the  $\text{H}\alpha$ , as would be the case if both pass through the same clouds of dust. However, in analogy to local starbursts, it may be the case that the UV and nebular line emission come from different regions in the galaxies and encounter different amounts of dust accordingly (Calzetti 1997). In particular, it has been suggested that the most massive stars are still embedded in the dust clouds in which they formed, leading to greater extinction of the nebular line emission. This may be the case with Q1623-BX376, which is bright in the rest-frame UV, with  $\text{Ly}\alpha$  emission and strong interstellar absorption lines, but which is undistinguished when observed in the rest-frame optical.

We can estimate the UV extinction using the observed broadband colors and an assumed spectral energy distribution (SED); we have calculated  $E(B-V)$  in this way, using the  $G-\mathcal{R}$  colors and an SED corresponding to continuous star formation with an age of 320 Myr, the median age found for LBGs at  $z \sim 3$  by Shapley et al. (2001). Because extinction corrections are highly sensitive to errors in color measurements, we have made an effort to quantify the uncertainties and biases in our photometry. We added a large number of artificial galaxies of known colors and magnitudes to the actual images, and then recovered them using the same photometric tools that we applied to the real data (see Adelberger 2002; Steidel et al. 2003). We then selected artificial galaxies whose recovered colors match our selection criteria, and sorted them into bins by color and  $\mathcal{R}$  magnitude. We used these to measure the mean and dispersion of  $\Delta(G-\mathcal{R}) = ((G-\mathcal{R})_{\text{meas}} - (G-\mathcal{R})_{\text{true}})$ , where the mean indicates systematic biases in the recovered colors and the dispersion reflects the characteristic measurement error,  $\sigma(G-\mathcal{R})$ . For the brightest galaxies in our sample ( $\mathcal{R} < 23.5$ ) both of these quantities are small:  $\langle \Delta(G-\mathcal{R}) \rangle \simeq 0.03$  and  $\sigma(G-\mathcal{R}) \simeq 0.05$ . For those with  $\mathcal{R} > 25$ , we find  $\langle \Delta(G-\mathcal{R}) \rangle \simeq 0.04$  and  $\sigma(G-\mathcal{R}) \simeq 0.14$ . For each galaxy in our sample, we have used these statistics to correct the measured  $G-\mathcal{R}$  color for the bias, and the color error has been propagated to determine uncertainties in  $E(B-V)$ ; these range from 0.03 for the brightest galaxies to 0.08 for the faintest.

After calculating  $E(B-V)$  in this way, we used the Calzetti et al. (2000) extinction law to correct the  $G$  magnitudes, and then used these to recalculate the UV star formation rates. For the sake of comparison we have also corrected the  $\text{H}\alpha$  fluxes, assuming the same values of  $E(B-V)$ ; we found this to give better agreement between the corrected UV and  $\text{H}\alpha$  SFRs than the Calzetti (1997) relation  $E_s(B-V) = (0.44 \pm 0.03)E_n(B-V)$  (where  $E_s(B-V)$  is the color excess of the stellar continuum and  $E_n(B-V)$  is that of the nebular emission lines). There may be some justification for this: if indeed there are galactic-scale outflows in these galaxies as in those at  $z \sim 3$ , then a screen of outflowing material may be obscuring all regions equally. Unfortunately we have no way of independently measuring the nebular extinction with our current data, as we do not have  $H$ -band measurements of  $\text{H}\beta$ . It should also be noted that the uncertainties inherent in flux calibration are too large to allow a reliable measurement of the Balmer decrement even if we had been able to obtain  $\text{H}\beta$  fluxes; for a Balmer decrement of 10%, expected for our mean  $E(B-V) = 0.10$  mag, we would need to measure each line flux with an accuracy of 5% or less, far better than our current capabilities. The issue is further complicated by the fact that  $\text{H}\alpha$  and  $\text{H}\beta$  lie in different bands and cannot be observed simultaneously, so there may be a systematic offset between the flux calibrations of the two observations. It will therefore be difficult to test the Calzetti model directly.

A comparison of the extinction-corrected SFRs is shown in the right panel of Figure 8. They are in better agreement than the uncorrected SFRs, with  $\langle \text{SFR}_{\text{H}\alpha}/\text{SFR}_{\text{UV}} \rangle = 1.2$  and a reduction in the scatter of 50% ( $1\sigma$ ; again accounting for the lower limits on four of the  $\text{H}\alpha$  SFRs). As emphasized above, the extinction correction is highly sensitive to uncertainties in the  $G-\mathcal{R}$  colors; the error bars reflect the errors in  $E(B-V)$  determined above, propagated through to the star formation rates. Not shown are uncertainties in the extinction law, flux calibrations, or conversion of flux to star formation rate, all of which are considerable. Given these sources of error, and the uncertainty in the value of  $E(B-V)$  that should be used for the nebular emission, the extinction-corrected SFRs should be taken with caution.

In Figure 9 we plot the ratio  $\text{SFR}_{\text{neb}}/\text{SFR}_{\text{UV}}$  against the rest frame UV continuum luminosity; none of these quantities have been corrected for extinction. We include data from Pettini et al. (2001), who used  $\text{H}\beta$  fluxes and the standard ratio  $\text{H}\alpha/\text{H}\beta = 2.75$  (Osterbrock 1989) to calculate SFRs from recombination lines in galaxies at  $z \sim 3$ . We have also included unpublished data from our NIRSPEC run in April 2001; these are LBGs at  $z \sim 3$ , and star formation rates have been calculated in the same way as in Pettini et al. (2001). These data will be discussed in detail in a future paper. The dotted curves represent lines of constant nebular line SFR, and the number at the top of each curve is its  $\text{SFR}_{\text{neb}}$ , in  $\text{M}_\odot \text{ yr}^{-1}$ . We see that there is a moderate trend for the UV-faint galaxies to have higher nebular line SFRs relative to their UV SFRs, as might be the case if these objects were more heavily reddened. From the curves of constant  $\text{SFR}_{\text{neb}}$  it can be seen that galaxies with similar nebular line luminosities and varying amounts of UV extinction will naturally follow such a trend. As noted in § 3, the UV luminosities of the galaxies in our sample vary by a factor of 9, while the  $\text{H}\alpha$  luminosities are the same to within a factor of 4; this is consistent with the idea that the galaxies in our sample have roughly the same SFR, but differ in the amount of UV extinction. This model may offer an explanation for the difference

between our results and those of Pettini et al. (2001), who observed no tendency for  $\text{SFR}_{\text{H}\beta}$  to be systematically greater than  $\text{SFR}_{\text{UV}}$ . As is apparent from the figure, the galaxies in their sample are brighter in the UV than all but four of those presented here, and could plausibly suffer less extinction. Several caveats are in order, however. We observe no correlation between either the  $(G-R)$  color or  $E(B-V)$  and the ratio of SFRs; if reddening is indeed the cause of the observed trend, then UV continuum measurements are not sufficient to quantify it. We also note that many objects with faint  $\text{H}\alpha$  emission would fall in the lower left corner of the plot; this is apparent when we add the objects we failed to detect to the figure (shown as magenta stars). We have plotted only those objects which were placed on the slit with another galaxy that was detected, so that we know our astrometry was correct. We have placed upper limits on their  $\text{H}\alpha$  star formation rates by assigning a maximum  $\text{SFR}_{\text{H}\alpha}$  corresponding to  $1\sigma$  less than the flux of our weakest detection, and we have calculated UV SFRs based on their photometry as with the rest of the sample. It is clear from this exercise that the absence of data points in the lower left is a selection effect; such galaxies would have undetectably small SFRs. The absence of data points in the upper right is more significant, as these objects would be easily detectable; from the curves of constant  $\text{SFR}_{\text{neb}}$ , we see that any galaxies falling here would have extremely large SFRs. In spite of these cautions, we believe that this figure is consistent with a model in which reddening is the primary cause of the discrepancy between the two SFR indicators.

Changes in the star formation rate on short timescales could also be reflected in our differing star formation rates, since  $\text{H}\alpha$  emission is a more instantaneous measure of the SFR than the UV emission. The nebular recombination lines are the reprocessed light of only the most massive ( $M \gtrsim 10\text{ M}_\odot$ ) and short-lived stars, while the UV emission probes a wider mass range ( $M \gtrsim 5\text{ M}_\odot$ ). Therefore a starburst which has begun in the past  $\sim 10^8$  yrs will not yet have reached full UV luminosity and will have an underestimated UV star formation rate, whereas a decline in star formation will cause an immediate decrease in  $\text{H}\alpha$  emission as the most massive stars die off. In a large sample of galaxies with redshifts  $0 < z < 0.4$ , Sullivan et al. (2000) find that the UV flux indicates a consistently higher SFR than the  $\text{H}\alpha$ , and that the discrepancy is best explained by short bursts of star formation superimposed on a smooth star formation history. Such a model could also explain the larger UV SFR of a galaxy such as Q1623-BX376; however, this relationship between the UV and  $\text{H}\alpha$  SFRs is strongest at the fainter end of the Sullivan et al. (2000) sample, whereas Q1623-BX376 would fall at the bright end. As noted above, there were several galaxies which we observed but failed to detect. This could be explained by a decline in the star formation rate, but due to the difficulties presented by the sky background in the IR, the marginal quality of some of our optical redshifts, and the possibility of errors in astrometry or the guiding and tracking of the instrument and telescope, these objects have not been included in the statistical comparison of SFRs.

In the following paragraphs we explain why we believe that a young stellar population is not the primary cause of the discrepancy between the SFRs. As we have no information on the ages of the stellar populations of the galaxies in our sample, we will assume that they are similar to LBGs at  $z \sim 3$ , although as we have pointed out above, the samples at  $z \sim 2$  and  $z \sim 3$  have different kinematic properties and the  $z \sim 3$  sample tends to cover

brighter UV luminosities. The stellar populations of LBGs at  $z \sim 3$  are now well-studied (Shapley et al. 2001; Papovich et al. 2001), and the Papovich et al. (2001) sample includes some galaxies in the range  $z = 2-2.5$ . Population synthesis models for a sample of 81 LBGs by Shapley et al. (2001) give a median age since the onset of the most recent episode of star formation of  $t_{\text{sf}} \simeq 320$  Myr, with more than 40% having  $t_{\text{sf}} > 500$  Myr and 25% having  $t_{\text{sf}} < 40$  Myr. We might then expect  $\sim 25\%$  of our sample to have an underestimated UV SFR; however, the youngest galaxies in the Shapley et al. (2001) sample are also the most extinguished and have the highest star formation rates. Among those with  $t_{\text{sf}} < 100$  Myr, the mean  $E(B-V)$  is 0.27, higher than that of any of the objects in our sample and  $3\sigma$  higher than our sample mean of 0.10. The mean star formation rate among the same subset is  $261\text{ M}_\odot\text{ yr}^{-1}$ , far higher than that of any of the objects in our sample even after correcting for extinction. Assuming that star-forming galaxies at  $z \sim 2$  are similar to those at  $z \sim 3$ , it is therefore unlikely that the stellar populations of our sample are young enough to account for the difference in SFRs.

Papovich et al. (2001) fit a set of detailed models to 33 LBGs in the Hubble Deep Field North, finding that the age distribution is strongly dependent on metallicity, IMF, the choice of extinction law, and the assumed star formation history. It is possible to vary these parameters to make the ages young enough to lead to an underestimate of the UV star formation rate; the youngest ages,  $\langle t \rangle \simeq 40$  Myr, are given by a Scalo IMF with  $0.2\text{ Z}_\odot$ . Although this may be a reasonable estimate for the metallicity of these objects—Pettini et al. (2001) find  $0.1$  to  $0.5\text{ Z}_\odot$  for galaxies at  $z \sim 3$ —the theoretical stellar atmospheres used in the population synthesis models are not well-tested for low metallicities, and the results should therefore be treated with caution. More generally, even ages as young as these cannot fully explain the discrepancy between the SFRs. The mean factor of 2.4 difference between the  $\text{H}\alpha$  and UV rates would require the average UV luminosity to have reached only  $\sim 40\%$  of its full value, which occurs less than 5 Myr after the beginning of a burst of continuous star formation. Such an extremely young age is unphysical; the time required for a burst of star formation to propagate across a galaxy is approximately the dynamical timescale, and  $t_{\text{dyn}} \simeq 30$  Myr for galaxies of the masses and sizes found in § 4. We can state the timescale argument in another way as well: the average stellar mass of our galaxies,  $\langle M \rangle \gtrsim 4 \times 10^{10}\text{ M}_\odot$ , combined with an assumed age of 2 Gyr gives a characteristic  $\dot{M} \sim 20\text{ M}_\odot\text{ yr}^{-1}$ , about the same as our mean  $\text{H}\alpha$  SFR of  $16\text{ M}_\odot\text{ yr}^{-1}$ . This implies that the current SFRs of the galaxies are similar to their past averages over the last 2 Gyr, and that a current burst is unlikely. Assuming an age younger than 2 Gyr, a mass larger than our lower limit of  $4 \times 10^{10}\text{ M}_\odot$ , or significant gas recycling results in a current SFR less than the past average, excluding a current burst even further.

The effects of dust and star formation history are indistinguishable in individual cases; in the sample taken as a whole, the systematic depression of  $\text{SFR}_{\text{UV}}$  relative to  $\text{SFR}_{\text{H}\alpha}$  suggests that extinction is the dominant effect, since variations in star formation history would induce scatter in the plots rather than systematic effects. Our knowledge of star formation and extinction at high redshift generally supports this conclusion. A moderate amount of extinction is indicated by our data, with a mean  $E(B-V)$  of 0.10 (corresponding to  $A_{1500} \sim 1$  mag and attenuation by a factor of  $\sim 2.5$ , using the Calzetti et al. (2000) extinc-

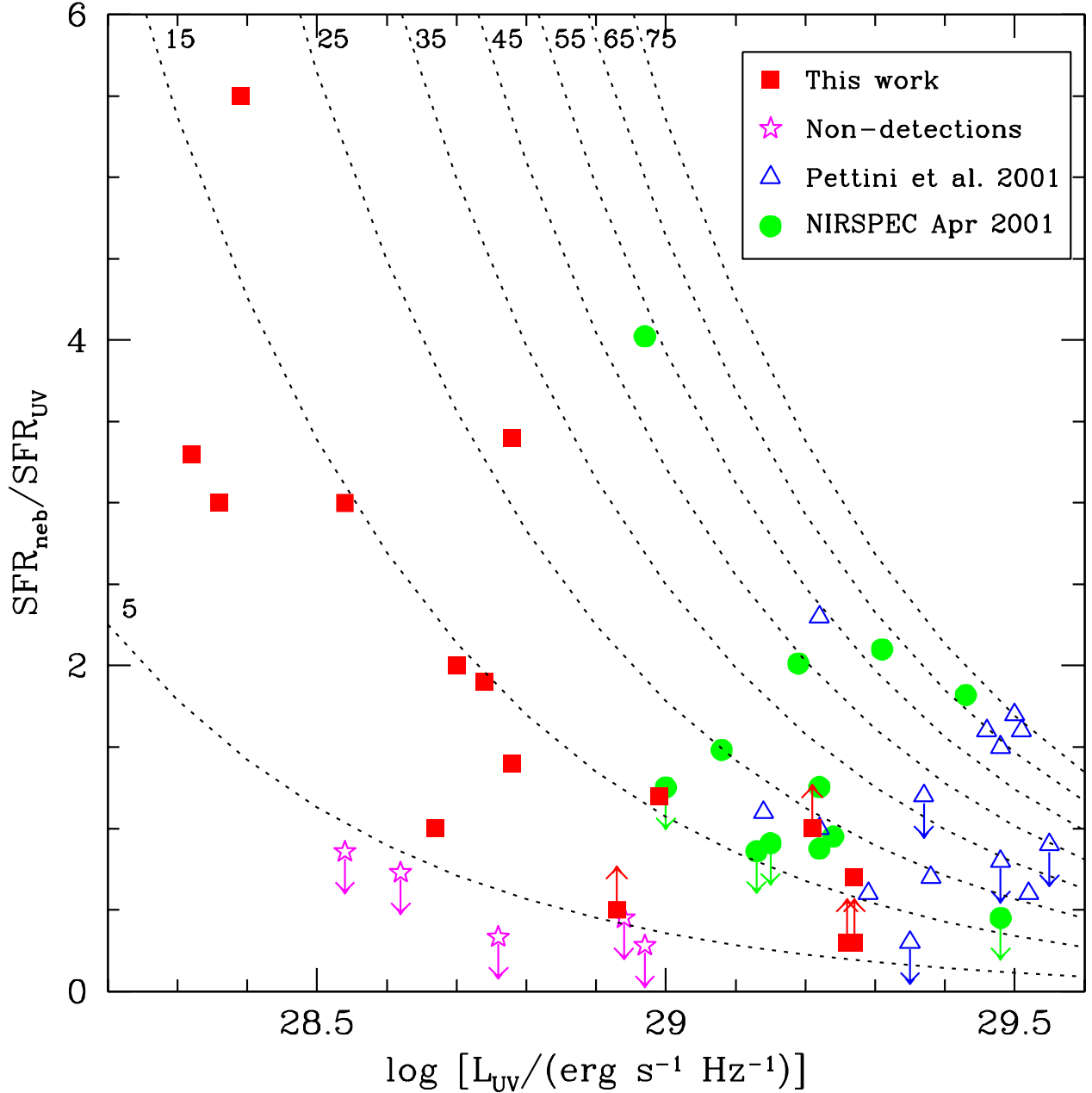


FIG. 9.— A comparison of the ratio of SFRs from nebular line and UV continuum emission with UV continuum luminosity. Red squares are the current data set, magenta stars represent upper limits on the ratio of SFRs for the five objects which we did not detect while successfully observing another galaxy on the same slit, blue triangles are from the  $z \sim 3$  sample of Pettini et al. (2001), and green circles are unpublished  $z \sim 3$  data from our April 2001 NIRSPEC run. The dotted curves are lines of constant  $SFR_{\text{neb}}$ , and the number at the top of each curve is its  $SFR_{\text{neb}}$  in  $M_{\odot} \text{ yr}^{-1}$ . UV luminosity is computed from the  $G$  magnitude for the  $z \sim 2$  sample; the center of the  $G$  filter corresponds to  $\sim 1500 \text{ \AA}$  at  $z = 2.3$ . For the  $z \sim 3$  sample we use the  $\mathcal{R}$  magnitude, corresponding to  $\sim 1700 \text{ \AA}$  at  $z = 3$ . SFRs for the Pettini et al. (2001) and April 2001 samples were calculated from  $H\beta$  emission, assuming  $H\alpha/H\beta = 2.75$  and applying the Kennicutt (1998) conversion from  $H\alpha$  to SFR. Errors are suppressed for clarity, but are  $\sim 25\%$  in  $SFR_{H\alpha}$  and 10% in  $SFR_{\text{UV}}$  and  $G$  as discussed in the text. See Pettini et al. (2001) for discussion of errors in the SFRs from  $H\beta$ .

tion law); in studies of LBGs at  $z \sim 3$ , Shapley et al. (2001) find a median dust attenuation factor of  $\sim 4.5$  at  $\sim 1500$  Å, while Papovich et al. (2001) find a factor of 3.0–4.4, depending on metallicity. Our results also provide some support for previous estimates of UV extinction at high redshift: if the  $\text{H}\alpha$  extinction is assumed to be about the same as it is in local galaxies, a typical factor of 2, and if we assume that the factor of  $\sim 2.4$  reduction in  $\text{SFR}_{\text{UV}}$  relative to  $\text{SFR}_{\text{H}\alpha}$  is due to extinction, then we obtain a UV extinction factor of  $\sim 5$ , the same as that applied to the UV luminosity density at  $z \sim 3$  by Steidel et al. (1999). We also note that this is in general agreement with the average UV attenuation factor of 5–6 obtained from studies of the X-ray luminosity of LBGs at  $z \sim 3$  (Nandra et al. 2002). In summary, while we cannot rule out the effects of star formation history entirely, our results are consistent with other estimates of extinction in galaxies at high redshift, and such extinction naturally explains the differences we see in the  $\text{H}\alpha$ - and UV-derived star formation rates.

## 6. SUMMARY AND CONCLUSIONS

We have presented  $\text{H}\alpha$  spectroscopy of 16 galaxies in the redshift range  $2.0 < z < 2.6$ ; this is so far the largest sample of near-IR spectra of galaxies at these redshifts. The galaxies were selected based on their broadband rest-frame UV colors, using an adaptation of the technique used to select Lyman break galaxies at  $z \sim 3$ . Those observed here are drawn from a large sample of such galaxies, with redshifts already confirmed; because proximity to a QSO sight-line was the primary selection criterion for near-IR observation, we believe the 16 galaxies presented here to be representative of the sample as a whole. We have analyzed the spectra in order to determine the kinematic and star-forming properties of the galaxies, and we reach the following conclusions.

1. Six of the 16 galaxies show spatially extended, tilted  $\text{H}\alpha$  emission lines, such as would be produced by ordered rotation. Rotation curves for these galaxies show a mean velocity of  $\sim 150$  km s $^{-1}$  at a mean radius of  $\sim 6$  kpc; these are lower limits obtained by taking half of the total range in both velocity and distance. Measuring from the spatial location of the continuum and the dynamical center of the lines, we obtain a maximum velocity of  $\sim 240$  km s $^{-1}$  and a maximum radius of 10 kpc in the most extreme cases. We have obtained archival *HST* images for two of these galaxies, and they appear to be morphologically irregular, as do all of the other galaxies in our sample for which we have such images. Because of their chaotic morphologies, we have not attempted to model any corrections to the rotation curves. We have used the lower limits on the rotational velocity and radius of each galaxy to derive a dynamical mass; we obtain a mean of  $\langle M \rangle \geq 4 \times 10^{10} \text{ M}_\odot$ . Because  $\text{H}\alpha$  emission probes only the central star-forming regions of the galaxies, we expect their total halo masses to be several times larger. These results are in general agreement with the predictions of models of hierarchical galaxy formation for LBGs at  $z \sim 3$ .

2. Values of the one-dimensional velocity dispersion  $\sigma$  range from 50 to 260 km s $^{-1}$ , with a mean of  $\sim 110$  km s $^{-1}$ . Assuming that the line widths are due to gravitational motions in

the potentials of the galaxies, the mean virial mass implied is  $2 \times 10^{10} \text{ M}_\odot$ ; this is in general agreement with the masses we obtain from the rotation curves. We consider other possible origins for the broadening of the lines, including large-scale outflows, mergers and interactions.

3. Both the rotational velocity  $v_c$  and the velocity dispersion  $\sigma$  tend to be larger at  $z \sim 2$  than at  $z \sim 3$ . We see evidence of rotation in  $\sim 40\%$  of our sample, whereas Pettini et al. (2001) found such evidence in only  $\sim 10\%$  of a sample of similar size at  $z \sim 3$ . Furthermore, we find rotational velocities of  $\sim 150$  km s $^{-1}$ , as compared to  $\sim 50$  km s $^{-1}$  at  $z \sim 3$ . Our mean value of  $\sigma$ ,  $\sim 110$  km s $^{-1}$ , is  $\sim 60\%$  larger than the value found at  $z \sim 3$  by Pettini et al. (2001). We have considered possible selection effects that may explain these systematic differences, but have not found a convincing explanation. It may be that the redshift dependence of surface brightness allows us to sample to larger radii at  $z \sim 2$ , or that our photometric selection criteria pick out different populations of galaxies at  $z \sim 2$  and  $z \sim 3$ . It is also possible that the effect is real and reflects the growth of disks between these two epochs.

4. We use the  $\text{H}\alpha$  luminosity to calculate the star formation rates of the galaxies, and compare these to the SFRs derived from the rest-frame UV continuum luminosity. We use the calibrations of Kennicutt (1998) in both cases. We obtain a mean  $\text{SFR}_{\text{H}\alpha}$  of  $16 \text{ M}_\odot \text{ yr}^{-1}$ , and a mean  $\text{SFR}_{\text{H}\alpha}/\text{SFR}_{\text{UV}}$  ratio of 2.4. After correcting both luminosities for extinction using the Calzetti et al. (2000) extinction law, we find  $\text{SFR}_{\text{H}\alpha}/\text{SFR}_{\text{UV}} = 1.2$ , with a 50% reduction in scatter. We discuss the effects of extinction and star formation history on the SFRs, and conclude that extinction is the more likely explanation for their discrepancy. We also see a moderate correlation between the ratio  $\text{SFR}_{\text{H}\alpha}/\text{SFR}_{\text{UV}}$  and the UV luminosities of the galaxies, such that UV-faint galaxies have a higher  $\text{SFR}_{\text{H}\alpha}/\text{SFR}_{\text{UV}}$  ratio. Such an effect could be produced if the fainter galaxies undergo more extinction.

5. Finally, we expect that many of the points discussed here will become clearer as the sample of near-IR observations of galaxies at these redshifts grows. The photometric technique for selecting galaxies at  $z \sim 2$  has so far produced hundreds of galaxies with confirmed redshifts in this range, and further observations of their kinematics, line fluxes, and morphologies will shed light on star formation, extinction, and the formation of disks at high redshift.

We would like to thank the referee for many helpful comments and suggestions. We also thank the staffs at the Keck and VLT observatories for their competent assistance with the observations. CCS, DKE, AES and MPH have been supported by grant AST-0070773 from the U.S. National Science Foundation and by the David and Lucile Packard Foundation. KLA acknowledges support from the Harvard Society of Fellows. Finally, we wish to extend special thanks to those of Hawaiian ancestry on whose sacred mountain we are privileged to be guests. Without their generous hospitality, most of the observations presented herein would not have been possible.

## REFERENCES

Adelberger, K. L. 2002, PhD thesis, California Institute of Technology  
 Adelberger, K. L. & Steidel, C. C. 2000, ApJ, 544, 218  
 Adelberger, K. L., Steidel, C. C., Giavalisco, M., Dickinson, M., Pettini, M., & Kellogg, M. 1998, ApJ, 505, 18  
 Adelberger, K. L., Steidel, C. C., Shapley, A. E., & Pettini, M. 2003, ApJ, 584, 45  
 Baugh, C. M., Cole, S., Frenk, C. S., & Lacey, C. G. 1998, ApJ, 498, 504  
 Bell, E. F. & Kennicutt, R. C. 2001, ApJ, 548, 681  
 Blain, A. W., Smail, I., Ivison, R. J., & Kneib, J.-P. 1999, MNRAS, 302, 632

Buat, V., Boselli, A., Gavazzi, G., & Bonfanti, C. 2002, A&A, 383, 801

Calzetti, D. 1997, AJ, 113, 162

Calzetti, D., Armus, L., Bohlin, R. C., Kinney, A. L., Koornneef, J., & Storchi-Bergmann, T. 2000, ApJ, 533, 682

Chapman, S. C., et al. 2000, MNRAS, 319, 318

Colina, L., Bohlin, R. C., & Castelli, F. 1996, Absolute Flux Calibration Spectrum of Vega (STScI Rep. OSG-CAL-96-01; Baltimore: STScI)

Conselice, C. J., Gallagher, J. S., Calzetti, D., Homeier, N., & Kinney, A. 2000, AJ, 119, 79

de Mello, D. F., Schaerer, D., Heldmann, J., & Leitherer, C. 1998, ApJ, 507, 199

Dickinson, M. 2000, Philosophical Transactions of the Royal Society of London, Series A, Vol. 358, no. 1772, p.2001, 358, 2001

Fan, X., et al. 2001, AJ, 121, 54

Feigelson, E. D. & Nelson, P. I. 1985, ApJ, 293, 192

Fruchter, A. S. & Hook, R. N. 2002, PASP, 114, 144

Genzel, R., Baker, A. J., Tacconi, L. J., Lutz, D., Cox, P., Guilloteau, S., & Omont, A. 2002, astro-ph/0210449

Giavalisco, M. & Dickinson, M. 2001, ApJ, 550, 177

Glazebrook, K., Blake, C., Economou, F., Lilly, S., & Colless, M. 1999, MNRAS, 306, 843

Hopkins, A. M., Connolly, A. J., & Szalay, A. S. 2000, AJ, 120, 2843

Johnson, K. E., Leitherer, C., Vacca, W. D., & Conti, P. S. 2000, AJ, 120, 1273

Kennicutt, R. C. 1998, ARA&A, 36, 189

Kobulnicky, H. A. & Koo, D. C. 2000, ApJ, 545, 712

Koekemoer, A. M. et al. 2002, "HST Dither Handbook", Version 2.0 (Baltimore: STScI)

Lançon, A., Goldader, J. D., Leitherer, C., & Delgado, R. M. G. . 2001, ApJ, 552, 150

Lavalley, M., Isobe, T., & Feigelson, E. 1992, in ASP Conf. Ser. 25: Astronomical Data Analysis Software and Systems I, Vol. 1, 245

Leitherer, C., Vacca, W. D., Conti, P. S., Filippenko, A. V., Robert, C., & Sargent, W. L. W. 1996, ApJ, 465, 717

Lemoine-Busserolle, M., Contini, T., Pello, R., Le Borgne, J.-F., Kneib, J.-P., & Lidman, C. 2002, A&A, in press (astro-ph/0210547)

Madau, P., Pozzetti, L., & Dickinson, M. 1998, ApJ, 498, 106

McLean, I. S., et al. 1998, in Proc. SPIE Vol. 3354, p. 566-578, Infrared Astronomical Instrumentation, Albert M. Fowler; Ed., Vol. 3354, 566-578

Mo, H. J., Mao, S., & White, S. D. M. 1998, MNRAS, 295, 319

—. 1999, MNRAS, 304, 175

Moorwood, A., et al. 1998, The Messenger, 94, 7

Moorwood, A. F. M., van der Werf, P. P., Cuby, J. G., & Oliva, E. 2003, Proceedings of the Workshop on The Mass of Galaxies at Low and High Redshift, eds. R. Bender and A. Renzini, Springer-Verlag, p. 302

Nandra, K., Mushotzky, R. F., Arnaud, K., Steidel, C. C., Adelberger, K. L., Gardner, J. P., Teplitz, H. I., & Windhorst, R. A. 2002, ApJ, 576, 625

Oke, J. B., et al. 1995, PASP, 107, 375

Osterbrock, D. E. 1989, Astrophysics of Gaseous Nebulae and Active Galactic Nuclei (Mill Valley: University Science Books)

Papovich, C., Dickinson, M., & Ferguson, H. C. 2001, ApJ, 559, 620

Pei, Y. C. 1995, ApJ, 438, 623

Pettini, M., Shapley, A. E., Steidel, C. C., Cuby, J., Dickinson, M., Moorwood, A. F. M., Adelberger, K. L., & Giavalisco, M. 2001, ApJ, 554, 981

Pettini, M., Steidel, C. C., Adelberger, K. L., Dickinson, M., & Giavalisco, M. 2000, ApJ, 528, 96

Schmidt, M., Schneider, D. P., & Gunn, J. E. 1995, AJ, 110, 68

Shapley, A. E., Steidel, C. C., Adelberger, K. L., Dickinson, M., Giavalisco, M., & Pettini, M. 2001, ApJ, 562, 95

Shapley, A. E., Steidel, C. C., Pettini, M., & Adelberger, K. L. 2003, ApJ, in press, astro-ph/0301230

Steidel, C. C., Adelberger, K. L., Giavalisco, M., Dickinson, M., & Pettini, M. 1999, ApJ, 519, 1

Steidel, C. C., Adelberger, K. L., Shapley, A. E., Pettini, M., Dickinson, M., & Giavalisco, M. 2003, ApJ, submitted

Steidel, C. C., Giavalisco, M., Pettini, M., Dickinson, M., & Adelberger, K. L. 1996, ApJ, 462, L17

Steidel, C. C. & Hamilton, D. 1993, AJ, 105, 2017

Steidel, C. C., Pettini, M., & Hamilton, D. 1995, AJ, 110, 2519

Sullivan, M., Treier, M. A., Ellis, R. S., Bridges, T. J., Milliard, B., & Donas, J. . 2000, MNRAS, 312, 442

Swaters, R. A., Madore, B. F., van den Bosch, F. C., & Balcells, M. 2002, astro-ph/0210152

Teplitz, H. I., Malkan, M., & McLean, I. S. 1998, ApJ, 506, 519

Tresse, L., Maddox, S. J., Le Fèvre, O., & Cuby, J.-G. 2002, MNRAS, 337, 369

Veilleux, S. & Osterbrock, D. E. 1987, ApJS, 63, 295

Vogt, N. P., Forbes, D. A., Phillips, A. C., Gronwall, C., Faber, S. M., Illingworth, G. D., & Koo, D. C. 1996, ApJ, 465, L15

Vogt, N. P., et al. 1997, ApJ, 479, L121

Yan, L., McCarthy, P. J., Freudling, W., Teplitz, H. I., Malumuth, E. M., Weymann, R. J., & Malkan, M. A. 1999, ApJ, 519, L47

TABLE 1  
GALAXIES OBSERVED

Galaxy	R.A. (J2000)	Dec. (J2000)	$z_{\text{Ly}\alpha}^{\text{a}}$	$z_{\text{abs}}^{\text{b}}$	$z_{\text{H}\alpha}^{\text{c}}$	$\mathcal{R}$	$G - \mathcal{R}$	Exposure (s)	Telescope/Instrument
CDFb-BN88	00:53:52.87	12:23:51.25	—	2.263	2.2615	23.14	0.29	$12 \times 720$	VLT 1/ISAAC
Q0201-B13	02:03:49.25	11:36:10.58	—	2.167	2.1663	23.34	0.02	$16 \times 720$	VLT 1/ISAAC
Westphal-BX600 <sup>d</sup>	14:17:15.55	52:36:15.64	—	—	2.1607	23.94	0.10	$5 \times 900$	Keck II/NIRSPEC
Q1623-BX376	16:25:05.63	26:46:49.12	2.415	2.408	2.4085	23.31	0.24	$4 \times 900$	Keck II/NIRSPEC
Q1623-BX428	16:25:48.42	26:47:40.24	—	2.053	2.0538 <sup>e</sup>	23.95	0.13	$4 \times 900$	Keck II/NIRSPEC
Q1623-BX432	16:25:48.74	26:46:47.05	2.187	2.180	2.1817	24.58	0.10	$4 \times 900$	Keck II/NIRSPEC
Q1623-BX447	16:25:50.38	26:47:14.07	—	2.149	2.1481	24.48	0.17	$4 \times 900$	Keck II/NIRSPEC
Q1623-BX449	16:25:50.55	26:46:59.63	—	2.417	2.4188	24.86	0.20	$4 \times 900$	Keck II/NIRSPEC
Q1623-BX511	16:25:56.10	26:44:44.38	—	2.246	2.2421 <sup>e</sup>	25.37	0.42	$4 \times 900$	Keck II/NIRSPEC
Q1623-BX522	16:25:55.76	26:44:53.17	—	2.476	2.4757	24.50	0.31	$4 \times 900$	Keck II/NIRSPEC
Q1623-MD107	16:25:53.88	26:45:15.19	2.543	2.536	2.5373	25.35	0.12	$4 \times 900$	Keck II/NIRSPEC
Q1700-BX691	17:01:05.99	64:12:10.27	—	2.189	2.1895	25.33	0.22	$4 \times 900$	Keck II/NIRSPEC
Q1700-BX717	17:00:57.00	64:12:23.71	2.438	—	2.4353	24.78	0.20	$4 \times 900$	Keck II/NIRSPEC
Q1700-MD103	17:01:00.20	64:11:56.00	—	2.308	2.3148	24.23	0.46	$900+600$	Keck II/NIRSPEC
Q1700-MD109	17:01:04.48	64:12:09.28	2.295	2.297	2.2942	25.46	0.26	$4 \times 900$	Keck II/NIRSPEC
SSA22a-MD41	22:17:39.97	00:17:11.04	—	2.173	2.1713	23.31	0.19	$15 \times 720$	VLT 1/ISAAC

<sup>a</sup>Vacuum heliocentric redshift of Ly $\alpha$  emission line, when present.

<sup>b</sup>Vacuum heliocentric redshift from rest-frame UV interstellar absorption lines.

<sup>c</sup>Vacuum heliocentric redshift of H $\alpha$  emission line.

<sup>d</sup>We have not yet obtained a rest-frame UV spectrum of Westphal-BX600.

<sup>e</sup>The H $\alpha$  redshifts of the galaxies Q1623-BX428 and Q1623-BX511 are somewhat uncertain due to the presence of strong sky lines near H $\alpha$ .

TABLE 2  
KINEMATICS

Galaxy	$z_{\text{H}\alpha}$ <sup>a</sup>	$\sigma$ (km s <sup>-1</sup> )	$v_c$ <sup>b</sup> (km s <sup>-1</sup> )	$M_{vir}$ <sup>c</sup> (M <sub>⊙</sub> )	$M_{dyn}$ <sup>d</sup> (M <sub>⊙</sub> )
CDFb-BN88	2.2615	$96 \pm 46$	—	$1.7 \times 10^{10}$	—
Q0201-B13	2.1663	$62 \pm 29$	—	$7.2 \times 10^9$	—
Westphal-BX600	2.1607	$181 \pm 24$	$\sim 210$	$6.2 \times 10^{10}$	$6.0 \times 10^{10}$
Q1623-BX376a	2.4085	$261 \pm 72$	—	$1.3 \times 10^{11}$	—
Q1623-BX376b	2.4085	$< 224$	—	$< 9.4 \times 10^{10}$	—
Q1623-BX428 <sup>e</sup>	2.0538	—	—	—	—
Q1623-BX432	2.1817	$51 \pm 22$	—	$5.0 \times 10^9$	—
Q1623-BX447	2.1481	$174 \pm 18$	$\sim 160$	$5.8 \times 10^{10}$	$3.0 \times 10^{10}$
Q1623-BX449	2.4188	$141 \pm 94$	—	$3.7 \times 10^{10}$	—
Q1623-BX511	2.2421	$152 \pm 47$	$\sim 80$	$4.4 \times 10^{10}$	$4.6 \times 10^9$
Q1623-BX522	2.4757	$< 44$	—	$< 3.8 \times 10^{10}$	—
Q1623-MD107	2.5373	$< 42$	—	$< 2.9 \times 10^{10}$	—
Q1700-BX691	2.1895	$170 \pm 18$	$\sim 220$	$5.5 \times 10^{10}$	$7.0 \times 10^{10}$
Q1700-BX717	2.4353	$< 60$	—	$< 1.3 \times 10^{10}$	—
Q1700-MD103	2.3148	$75 \pm 21$	$\sim 100$	$1.1 \times 10^{10}$	$1.6 \times 10^{10}$
Q1700-MD109	2.2942	$87 \pm 35$	—	$1.5 \times 10^{10}$	—
SSA22a-MD41	2.1713	$107 \pm 15$	$\sim 150$	$2.2 \times 10^{10}$	$4.2 \times 10^{10}$

<sup>a</sup>Vacuum heliocentric redshift of H $\alpha$  emission line.

<sup>b</sup>Minimum rotational velocity,  $(v_{\text{max}} - v_{\text{min}})/2$ .

<sup>c</sup>Masses calculated from the velocity dispersion.

<sup>d</sup>Minimum masses derived from rotational velocities when available.

<sup>e</sup>Sky line contamination prevented a measurement of  $\sigma$ .

TABLE 3  
FLUXES AND STAR FORMATION RATES

Galaxy	$z_{\text{H}\alpha}$ <sup>a</sup>	$\mathcal{R}$	$G - \mathcal{R}$	$F_{\text{H}\alpha}$ <sup>b</sup>	$L_{\text{H}\alpha}$ <sup>c</sup>	$E(B - V)$ <sup>d</sup>	$\text{SFR}_{\text{H}\alpha}$ <sup>e</sup>	$\text{SFR}_{\text{H}\alpha}$ <sup>f</sup>	$\text{SFR}_{\text{UV}}$ <sup>g</sup>	$\text{SFR}_{\text{UV}}$ <sup>h</sup>	$\frac{\text{SFR}_{\text{H}\alpha}}$ <sup>i</sup> $\text{SFR}_{\text{UV}}$
CDFb-BN88	2.2615	23.14	0.29	2.6	1.0	0.146	$> 8$	$> 14$	$26 \pm 3$	$106^{+31}_{-24}$	$> 0.3$
Q0201-B13	2.1663	23.34	0.02	2.4	0.8	0.004	$> 7$	$> 7$	$26 \pm 3$	$27^{+6}_{-5}$	$> 0.3$
Westphal-BX600	2.1607	23.94	0.10	6.3	2.2	0.048	$17 \pm 4$	$21^{+3}_{-3}$	$14 \pm 1$	$22^{+11}_{-7}$	1.2
Q1623-BX376	2.4085	23.31	0.24	5.3	2.4	0.111	$19 \pm 5$	$29^{+3}_{-3}$	$26 \pm 3$	$84^{+27}_{-20}$	0.7
Q1623-BX428	2.0538	23.95	0.13	2.7	0.8	0.073	$> 6$	$> 9$	$12 \pm 1$	$25^{+12}_{-8}$	$> 0.5$
Q1623-BX432	2.1817	24.58	0.10	5.4	1.9	0.048	$15 \pm 4$	$18^{+4}_{-3}$	$8 \pm 1$	$13^{+8}_{-5}$	1.9
Q1623-BX447	2.1481	24.48	0.17	5.6	1.9	0.082	$15 \pm 4$	$21^{+5}_{-4}$	$8 \pm 1$	$18^{+12}_{-7}$	1.9
Q1623-BX449	2.4188	24.86	0.20	1.8	0.8	0.094	$6 \pm 2$	$9^{+2}_{-2}$	$6 \pm 1$	$18^{+15}_{-8}$	1.0
Q1623-BX511	2.2421	25.37	0.42	3.4	1.3	0.194	$10 \pm 3$	$22^{+8}_{-6}$	$3 \pm 0.3$	$22^{+28}_{-12}$	3.3
Q1623-BX522	2.4757	24.50	0.31	2.8	1.3	0.132	$11 \pm 3$	$18^{+4}_{-3}$	$8 \pm 1$	$35^{+26}_{-15}$	1.4
Q1623-MD107	2.5373	25.35	0.12	3.7	1.9	0.043	$15 \pm 4$	$18^{+6}_{-4}$	$5 \pm 1$	$8^{+9}_{-4}$	3.0
Q1700-BX691	2.1895	25.33	0.22	7.7	2.8	0.108	$22 \pm 6$	$33^{+12}_{-9}$	$4 \pm 0.4$	$10^{+12}_{-7}$	5.5
Q1700-BX717	2.4353	24.78	0.20	3.8	1.8	0.087	$14 \pm 4$	$20^{+5}_{-4}$	$7 \pm 1$	$18^{+15}_{-8}$	2.0
Q1700-MD103	2.3148	24.23	0.46	8.2	3.4	0.224	$27 \pm 7$	$64^{+13}_{-11}$	$8 \pm 1$	$88^{+56}_{-35}$	3.4
Q1700-MD109	2.2942	25.46	0.26	2.8	1.1	0.124	$9 \pm 2$	$14^{+5}_{-4}$	$3 \pm 0.3$	$12^{+14}_{-6}$	3.0
SSA22a-MD41	2.1713	23.31	0.19	7.9	2.8	0.097	$> 22$	$> 32$	$23 \pm 2$	$61^{+20}_{-15}$	$> 1.0$
Mean value <sup>j</sup>	2.2787	24.37	0.21	4.6	1.8	0.101	16	26	12	35	2.4

<sup>a</sup>Vacuum heliocentric redshift of H $\alpha$  line.

<sup>b</sup>Line flux in units of  $10^{-17}$  erg s $^{-1}$  cm $^{-2}$ .

<sup>c</sup>Luminosity in units of  $10^{42}$  erg s $^{-1}$ .

<sup>d</sup>From  $G - \mathcal{R}$  colors, corrected as described in § 5.

<sup>e</sup>SFR in  $\text{M}_{\odot}$  yr $^{-1}$  from H $\alpha$  luminosity, uncorrected for extinction.

<sup>f</sup>SFR in  $\text{M}_{\odot}$  yr $^{-1}$  from H $\alpha$  luminosity, corrected for extinction.

<sup>g</sup>SFR in  $\text{M}_{\odot}$  yr $^{-1}$  from  $G$  magnitude, uncorrected for extinction.

<sup>h</sup>SFR in  $\text{M}_{\odot}$  yr $^{-1}$  from  $G$  magnitude, corrected for extinction.

<sup>i</sup>Ratio of uncorrected SFRs.

<sup>j</sup>For those quantities containing lower limits, statistics are computed using survival analysis as discussed in § 5.

Note. —  $H_0 = 70$  km s $^{-1}$  Mpc $^{-1}$ ,  $\Omega_m = 0.3$ , and  $\Omega_{\Lambda} = 0.7$ .